Research Square

Preprints are preliminary reports that have not undergone peer review.
They should not be considered conclusive, used to inform clinical practice,
or referenced by the media as validated information.

Faulting and Hydrothermal Alteration in a Proterozoic Rapakivi Batholith: Coupling Geothermal Reservoir Formation and Element Mobility

Alan Bischoff

alan.bischoff@utu.fi

University of Turku

Jussi S. Heinonen

Åbo Akademi University

Michael J. Heap

Université de Strasbourg, CNRS, Institut Terre et Environnement de Strasbourg

Jaakko Kara

University of Turku

Patrik Jänkävaara

University of Turku

Daniel Carbajal-Martínez

Geological Survey of Finland (GTK)

Leonardo Salazar

Thermo Fisher Scientific (Australia)

Thierry Reuschlé

Université de Strasbourg, CNRS, Institut Terre et Environnement de Strasbourg

Ester M. Jolis

Geological Survey of Finland (GTK)

Luana M. Florisbal

Federal University of Santa Catarina

Sören Fröjdö

Åbo Akademi University

Nicklas Nordbäck

Geological Survey of Finland (GTK)

Jukka Kuva

Geological Survey of Finland (GTK)

Research Article

Keywords: Geothermal reservoirs, Fault zones, Critical elements, Hydrothermal alteration, Fennoscandian Shield

Posted Date: November 2nd, 2026

DOI: https://doi.org/10.21203/rs.3.rs-11313877/v1

License: This work is licensed under a Creative Commons Attribution 4.0 International License. Read Full License

Additional Declarations: No competing interests reported.

Faulting and Hydrothermal Alteration in a Proterozoic Rapakivi Batholith: Coupling Geothermal Reservoir Formation and Element Mobility

Alan Bischoff[1], Jussi S. Heinonen[2], Michael J. Heap[3,4], Jaakko Kara[1], Patrik Jänkävaara[1], Daniel Carbajal-Martínez[5], Leonardo Salazar[6], Thierry Reuschlé[3], Ester M. Jolis[5], Luana M. Florisbal[7], Sören Fröjdö[2], Nicklas Nordbäck[5], Jukka Kuva[5]

[1] University of Turku, Finland
[2] Åbo Akademi University, Finland
[3] Université de Strasbourg, CNRS, Institut Terre et Environnement de Strasbourg, France
[4] Institut Universitaire de France (IUF), France
[5] Geological Survey of Finland (GTK), Finland
[6] Thermo Fisher Scientific, Australia
[7] Federal University of Santa Catarina, Brazil

E-mail: alan.bischoff@utu.fi

AB: 0000-0002-4890-0193
DC-M: 0000-0002-5130-4886
MJH: 0000-0002-4748-735X
EMJ: 0009-0005-2950-7379
PJ: 0009-0002-8462-9705
JSH: 0000-0001-8998-4357
LS:
TH:
SF:
LMF: 0000-0001-6580-5828
NN: 0000-0002-7152-7550
JK: 0000-0003-0081-4111

Abstract

Crystalline rocks are increasingly recognized as geothermal targets, where reservoir parameters including porosity and permeability strongly reflect the coupled effects of brittle deformation and hydrothermal alteration. To quantify how these effects modify reservoir properties in crystalline rocks, we integrate petrophysical, mineralogical, geochemical, geochronological, and structural data from the well exposed Vehmaa Rapakivi Batholith in southwestern Finland, an analogue for fault-hosted geothermal reservoirs in crystalline settings. The batholith records five alteration stages: (1) late-magmatic F-rich, (2) high-temperature cementation, (3) propylitic alteration, (4) quartz cementation, and (5) low-temperature oxidizing overprint. The strongest reservoir development is associated with Stage 3, where mineral dissolution, replacement, and microfracturing generated porosities of up to 18%, whereas Stage 2 produced dense cemented rocks with little preserved porosity. Subsequent quartz cementation and low-temperature oxidizing alteration further modified reservoir properties through localized mineral dissolution and fracture sealing. U-Pb ages of titanite and zircon confirm that Stages 1 and 2 began during the late crystallization to early cooling of the batholith at ~1.57 Ga, while a younger ~1.0 Ga age suggests much later fluid circulation or thermal resetting. Notably, kilometer-scale strike-slip faults and alteration networks transect much of the batholith, indicating that these processes can operate over rock volumes relevant to geothermal development. These processes also redistributed economically relevant elements, including REE, Sc, Sr, Sn, and Zn concentrated along the faults. Our results show that fracturing, dissolution, and cementation control crystalline reservoir quality, while fluid–rock reactions govern element mobility and mineralization, linking geothermal potential with critical element resources.

Highlights

- Fault-controlled alteration creates or destroys crystalline reservoirs through competing dissolution, fracturing, and cementation.
- Kilometer-scale alteration zones in the Vehmaa Batholith record hydrothermal activity from ~1.57 to ~1.0 Ga.
- Long-lived fluid–rock interaction couples geothermal reservoir development with redistribution and enrichment of critical elements.

Keywords: Geothermal reservoirs, Fault zones, Critical elements, Hydrothermal alteration, Fennoscandian Shield

1 Introduction

Understanding geothermal reservoirs in crystalline settings requires explaining how an initially compact, low-porosity rock develops connected fluid pathways and how subsequent geological processes modify them. In such systems, mineral alteration and element mobility are closely coupled to reservoir evolution, because processes such as mineral dissolution, replacement, and precipitation can both redistribute chemical components and modify pore and fracture networks through time.

Although crystalline basement rocks have traditionally been regarded as poor geothermal targets because of their low primary porosity and limited matrix permeability (e.g., Manning and Ingebritsen, 1999; Jolie et al., 2021), secondary processes such as fracturing, hydrothermal alteration, and metasomatism can substantially enhance reservoir potential, in cases producing porosities of up to ~30% and permeabilities exceeding the 10^{-12} m² (~1 Darcy) order (e.g., Caspari et al., 2020; Kraal et al., 2021; Harpers et al., 2024; Bischoff et al., 2024; Carbajal-Martinez et al., 2026). Today, the significance of fractured and altered crystalline reservoirs extends beyond geothermal energy, as they are also emerging targets for the extraction of critical elements and high-density energy gases from geothermal fluids, including lithium, helium, and hydrogen resources whose recoverability is ultimately controlled by the porosity and permeability of reservoir rocks (Sanjuan et al., 2022; Sajkowski et al., 2023). This resource can also include the presence of rare earth elements (REEs; e.g., La, Ce, Nd, Y, and Eu), metals such as Sn, Cu, and Zn, and other critical material including Nb, Ta, Zr, Hf that may become enriched within

hydrothermally altered crystalline rocks, particularly in association with large-scale fault system (e.g., Sibson, 1996; Cox, 2005; Migdisov et al., 2016; Sanchez-Alfaro et al., 2016). Similarly, understanding fluid flow and geochemical alteration within crystalline rocks is particularly relevant to the long-term safety of geological repositories for spent nuclear fuel, as demonstrated at the Olkiluoto site in southwestern Finland (Viola et al., 2011; Aaltonen et al., 2018; Kuva et al., 2012).

The Vehmaa Rapakivi Batholith in southwestern Finland (Figure 1) provides an exceptional case-study to investigate the coupled effects of fault-related hydrothermal alteration on the petrophysical, thermal, and geochemical signature of crystalline reservoirs. This Mesoproterozoic intrusion was emplaced at shallow crustal depths of approximately 3–5 km within Paleoproterozoic Svecofennian gneisses and migmatites (Eklund & Shebanov, 1999) and subsequently experienced multiple episodes of brittle faulting and hydrothermal alteration, producing substantial structural and mineralogical modification along the fault zones (Nordbäck et al., 2026).

In Part 1 of this study (Nordbäck et al., 2026), we demonstrated that the Vehmaa Batholith is transected by two major strike-slip fault systems that control the spatial distribution of kilometer-scale fracture networks and hydrothermal alteration zones. Building on this structural framework, the present paper (Part 2) examines how fault-controlled fluid circulation modified the mineralogy, geochemistry, porosity, permeability, and other reservoir properties of the granite. By integrating a multidisciplinary approach that combines mineralogical and geochemical analyses (thin-section petrography, SEM–EDS, XRD, XRF) with microstructural imaging (XCT, mineral maps), U–Pb geochronology of alteration minerals, and petrophysical tests, this study aims to: (i) characterize mineral alteration pathways and their impacts on key petrophysical properties that govern the

performance of geothermal reservoirs, (ii) assess the resulting changes in the geochemical, physical, and thermal properties of crystalline rocks transected by faults, and (iii) investigate the mechanisms driving the formation and evolution of fracture–altered Rapakivi reservoirs in the Fennoscandian Shield over geological timescales.

The results of our work advance understanding of post magmatic faulting coupled with hydrothermal alteration in crystalline terranes, offering transferable insights for geothermal exploration, the potential co-production of critical elements for the energy transition, and the long-term evolution of fluid pathways relevant to the safety assessment of deep geological repositories for nuclear waste.

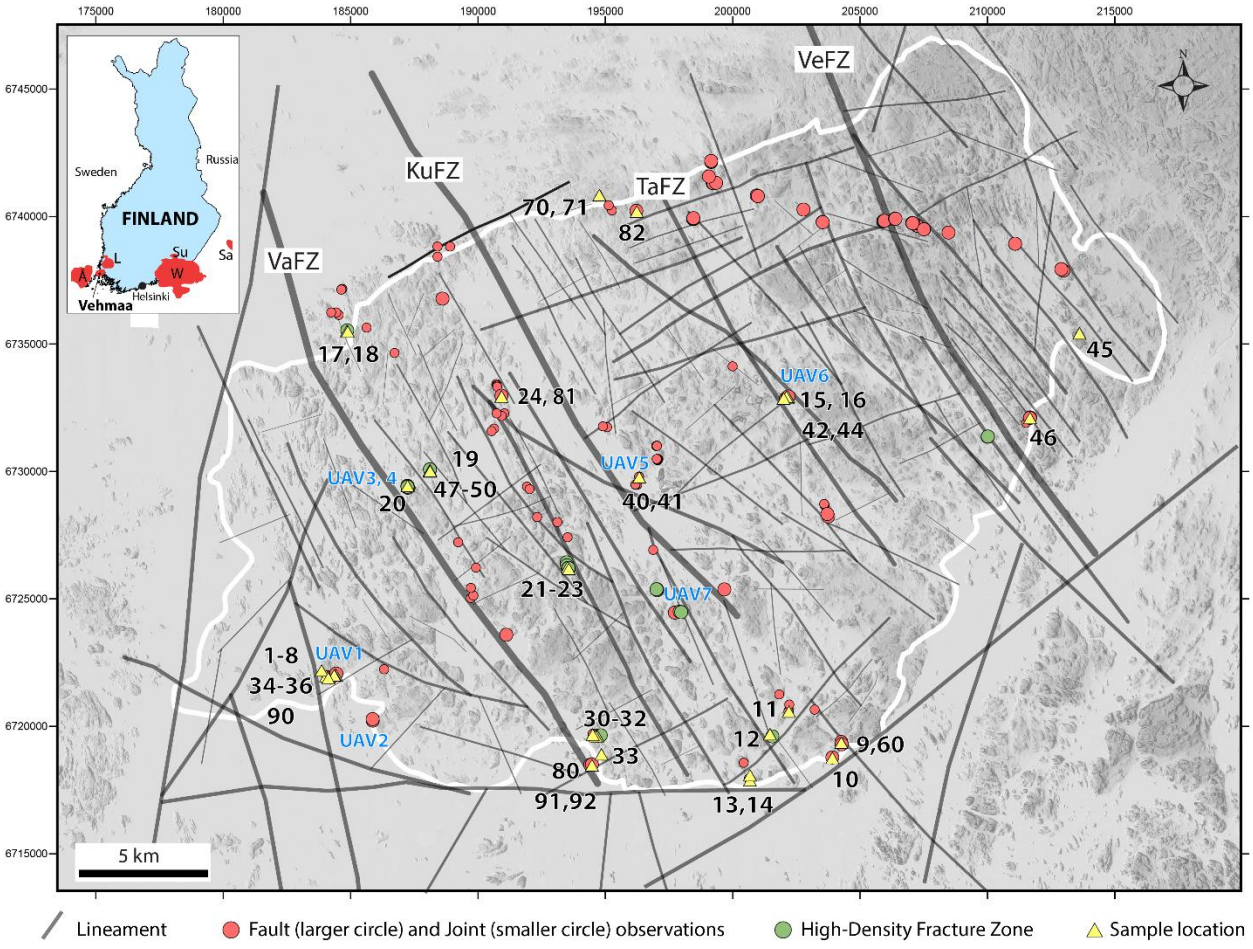


Figure 1: Location and structural framework of the Vehmaa Rapakivi Batholith, southwestern Finland. The inset map shows the position of the batholith within the Fennoscandian Shield. The main panel presents a LiDAR-derived topographic map highlighting the major brittle fault systems transecting the batholith after Nordbäck et al., 2026. Sample locations analyzed in this study are indicated by black numbers corresponding to sample codes. The Vuosnainen geochemical transect is located at the UAV1 site (sample KUS-090). Fault abbreviations: VaFZ = Vartsala Fault Zone; KuFZ = Kustavi Fault Zone; TaFZ = Taivassalo Fault Zone; VeFZ = Vehmaa Fault Zone. Rapakivi granite abbreviations: Å = Åland Batholith; L = Laitila Batholith; W = Wiborg Batholith; Sa = Salmi Batholith; Su = Suomenniemi Intrusive Complex.

2 Geological Setting

Southern Finland forms part of the Fennoscandian Shield and is mainly composed of Paleoproterozoic granites, migmatites, and supracrustal rocks that were largely deformed under high-grade metamorphic conditions during the Svecofennian Orogeny (1.9–1.8 Ga; Lahtinen et al. 2009; Nironen, 1997). Svecofennian ductile shear-zones were active until ~1.79 Ga, after which deformation progressively became brittle. The earliest recognized brittle phase occurred at ~1.75 Ga and involved reactivation of inherited structures and development of new faults under broadly NW–SE to NNW–SSE transpressional conditions (Väisänen and Skyttä, 2007; Mattila and Viola, 2014).

The Meso- to Neoproterozoic evolution of southern Finland (~1.67–0.9 Ga) records a prolonged period of intracratonic tectonic reorganization, involving episodic extension (Korja et al., 1993), bimodal magmatism (Rämö and Haapala, 1995), sedimentation, and mafic dike intrusions (Suominen, 1991; Pokki et al., 2013), along with episodes of far-field compressional deformation (Åhäll et al., 2000; Nordbäck et al., 2024). During the early stages of this evolution (~1.67–1.54 Ga), E–W to NW–SE extension was accompanied by widespread A-type rapakivi magmatism and the emplacement of large batholiths, including Vehmaa, Laitila, Åland, and Wiborg (Rämö, 1991; Nironen, 1997). Although traditionally interpreted as anorogenic, rapakivi magmatism has also

been linked to distal geodynamic effects of the Gothian orogenesis along the western margin of the Fennoscandian Shield (Åhäll et al., 2000). In the Vehmaa Batholith, zircon and monazite from different granitic facies yield U–Pb ages of 1582 ± 4 Ma and 1573 ± 8 Ma, respectively, which, together with crosscutting relationships between the different granite facies, indicate successive crystallization events rather than a single homogeneous magmatic pulse (Selonen et al., 2005). Crystallization temperatures are estimated at ~700–800 °C, based on thermobarometric constraints associated with the development of the rapakivi texture (Eklund and Shebanov, 1999).

Following emplacement of the rapakivi batholiths, southwestern Finland underwent several phases of brittle deformation. Two principal Mesoproterozoic strike-slip phases have been recognized in the Vehmaa and Åland rapakivi batholiths: (i) an older phase at approximately 1.55–1.4 Ga, associated with broadly NW–SE- compression, and (ii) a younger phase at approximately 1.3–1.2 Ga, associated with NE–SW compression (Nordbäck et al., 2024, 2026). The youngest recognized major fault system in southwestern Finland comprises low-angle thrusts attributed to the Sveconorwegian orogeny at approximately 1.1 Ga, after which deformation was limited to minor reactivation and the region evolved into a relatively stable cratonic domain by ~900 Ma (Mattila and Viola, 2014; Nordbäck et al., 2022; Green et al., 2022).

3 Subsolidus alteration of rapakivi granites in southern Finland

Rapakivi granites in southern Finland preserve a wide range of alteration processes often interpreted to result from fluids released during the final stages of magma crystallization and subsequent hydrothermal circulation. For example, in the Kymi topaz granite, crystallization of an evolved F-rich residual melt at ~600–700 °C was followed by episodic fluid exsolution and hydrothermal alteration, producing miarolitic cavities, pegmatites, greisens, and mineralized veins

containing Pb, Zn, Cu, As, W, and S (Haapala and Lukkari, 2005; Lukkari et al., 2009; Berni et al., 2017, 2020). A different style of high-temperature alteration is recorded in the Suomenniemi rapakivi complex, where clinopyroxene bearing episyenites formed through interaction of the granite with oxidizing, Na-rich fluids at near solidus temperatures above ~650 °C. This alteration involved extensive quartz removal, sodium metasomatism, feldspar recrystallization, and element redistribution, locally producing substantial changes in rock volume and generating secondary porosity (Suikkanen et al., 2019; Abersteiner et al., 2025).

Following the high-temperature alteration associated with the Mesoproterozoic rapakivi magmatism, southern Finland underwent repeated hydrothermal circulation at temperatures ranging from slightly above 300 °C to below 100 °C. These alteration events are associated with the widespread occurrence of chlorite, epidote, sericite, calcite, and sulphides veins along fractures and are interpreted to reflect repeated tectonic reactivation, including post-rapakivi strike-slip deformation at ~1.55–1.40 Ga, renewed compression and diabase emplacement at ~1.3–1.2 Ga, and subsequent fault reactivation during the Sveconorwegian orogeny at ~1.1–0.9 Ga (Viola et al., 2014; Aaltonen et al., 2018; Nordbäck et al., 2022).

A much younger episode of hydrothermal circulation is recorded by fluorite–calcite–galena veins in the Lovisa area of the Wiborg Batholith, where saline fluids are interpreted to have circulated at ~60–190 °C. Preliminary Sm–Nd fluorite ages around 400 Ma suggest remobilization of Ca, F, and Pb from the Precambrian basement during the Paleozoic, potentially in response to Caledonian tectonic activity (Alm et al., 2005). Thermochronological data further indicate that the southern Finland Precambrian basement was also affected by Phanerozoic burial and exhumation, reaching maximum paleotemperatures of ~60 ± 10 °C near the Carboniferous–Permian boundary, while mobilization and precipitation of calcite, fluorite, and Pb-Zn sulphides-bearing veins are

188 interpreted to result from hydrothermal circulation during the Devonian and related to the far-field
189 effects of the Caledonian orogeny (Kukkonen et al., 2025). Even younger alteration and
190 mineralization processes are inferred at Olkiluoto, where fracture-filled calcite records
191 groundwater evolution linked to marine-water infiltration, indicating continued mineral–fluid
192 interaction into the Quaternary (Sahlstedt et al., 2010).

193 # 4 Samples and Methods

194 A total of 49 representative hand samples were collected from key rock facies of the Vehmaa
195 Rapakivi Batholith (Figure 1), encompassing relatively unaltered rapakivi granites and fault-
196 controlled zones affected by variable degrees of fracturing and alteration. Our analytical workflow
197 integrated petrophysical measurements, mineralogical and pore-space characterization, whole-
198 rock geochemistry, microstructural analysis, and isotopic dating of secondary alteration minerals.
199 The methods included detailed thin-section petrography, scanning electron microscopy coupled
200 with X-ray spectroscopy (SEM–EDS), X-ray diffraction (XRD), automated elemental and
201 mineralogical mapping, X-ray computed tomography (XCT), whole-rock major- and trace-
202 element analysis by X-ray fluorescence (XRF), and U-Pb geochronology of zircon and titanite by
203 LA-ICP-MS to constrain the timing of magmatic crystallization and subsequent alteration.
204 Detailed description of the sample preparation, analytical conditions, and instrument
205 specifications, are provided in the Supplementary Material.

206 In addition, a 122 cm-long transect sample (KUS-090) was collected across a NW-trending strike-
207 slip fault at Vuosnainen, corresponding to site AUV1 in Figure 1. From this transect, nine
208 representative subsamples were systematically collected to characterize geochemical variations
209 across the fault zone architecture (Figure 2). Diverse elements of the fault zone were defined from

outcrop relationships, combining structural position, fracture geometry, and alteration intensity. The fault core corresponds to the narrow central area containing the most intensely fractured and altered material, spatially associated with the principal displacement zone (PDZ) of the strike-slip fault. The core is bounded by two principal fault strands labelled DZ1 and DZ2 in Figure 2, defined by structures including antithetic faults and extensional fractures, together with a visible alteration halo. Outside the fault core and damage zones, the rock forms the host block (HB), which consists of massive, weakly altered granite where fracture density and alteration intensity decrease markedly.

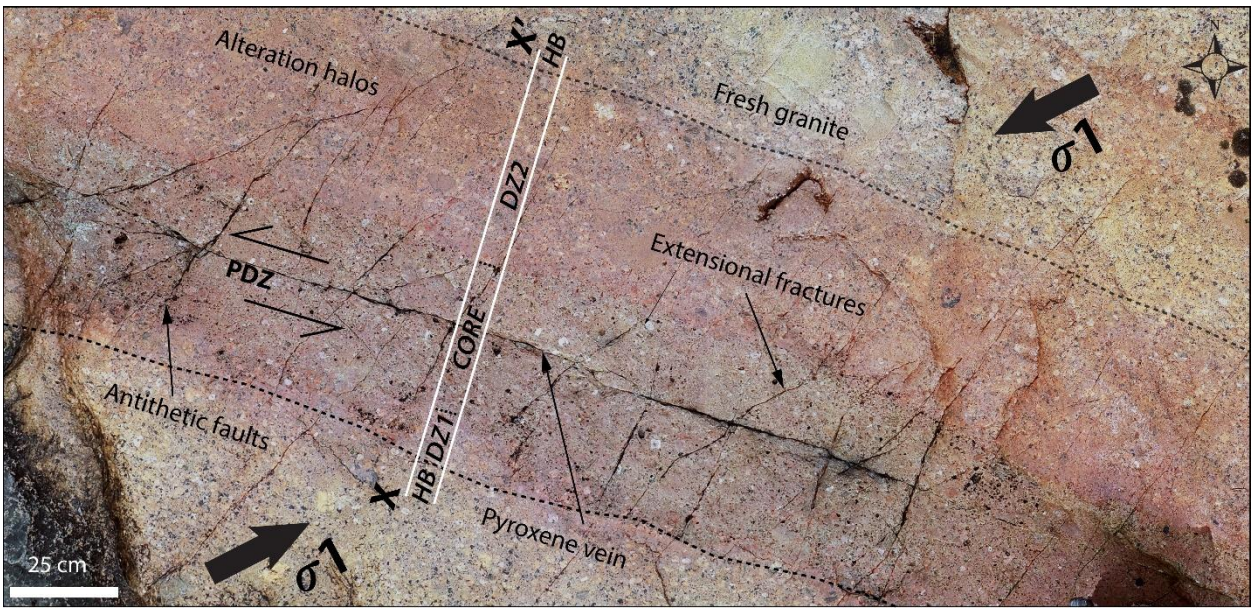
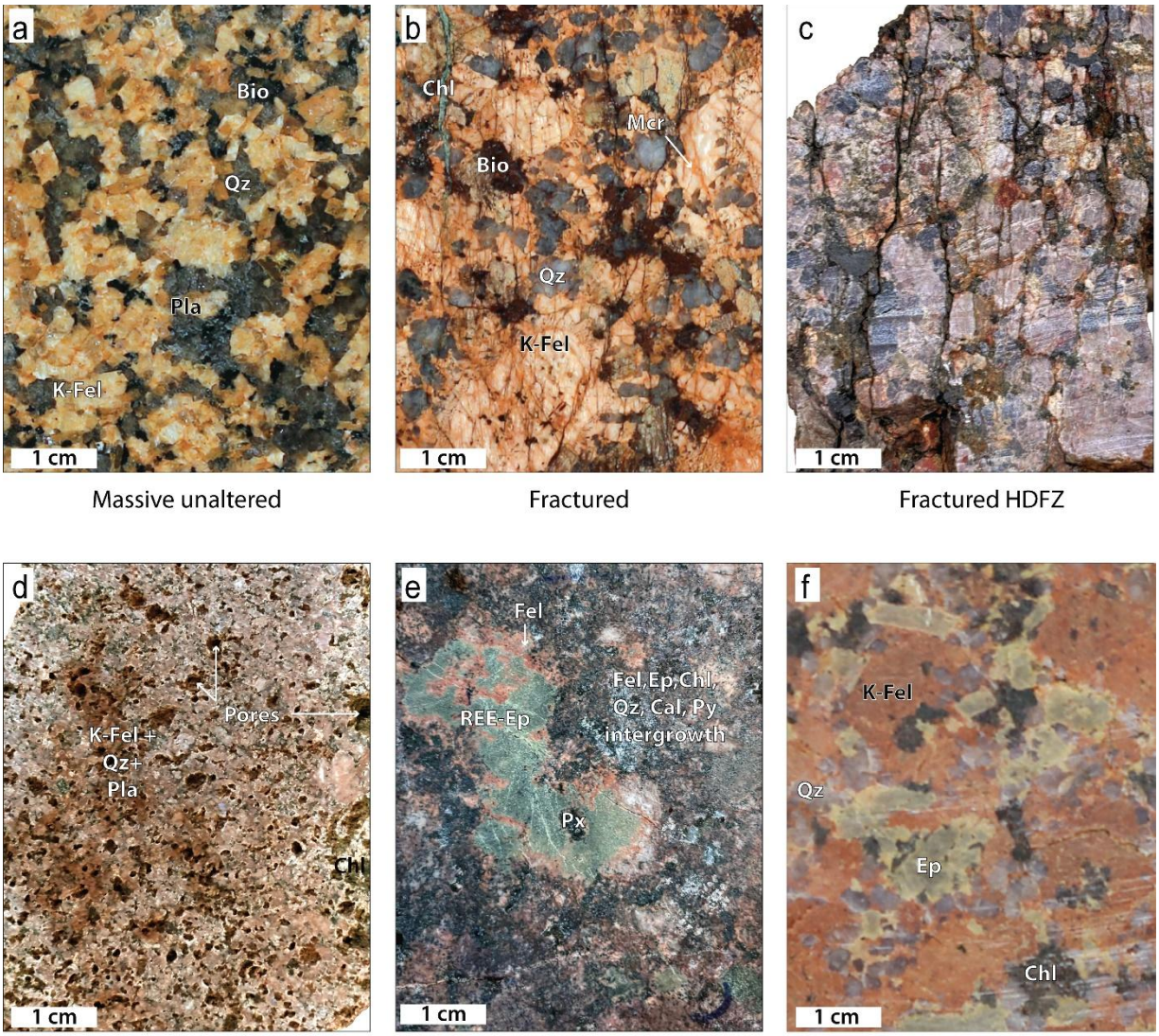


Figure 2: Outcrop-scale architecture of a subsidiary NW-trending sinistral strike-slip fault at Vuosnainen. The X–X′ line marks the 122 cm-long transect sample collected to characterize geochemical variations across from the fault zone.

5 Results

5.1 Lithofacies

Mineralogical and textural characteristics of representative samples from the Vehmaa Rapakivi Batholith reveal a transition from pristine granites to highly altered and porous granites. Porosity development, mineral replacement, and cementation vary systematically with the proximity to major strike-slip faults, consistent with the structural framework documented in the first part of this study (Nordbäck et al., 2026). Three main lithofacies are distinguished: (i) massive granites showing little to no alteration, (ii) fractured granites, in which fracturing represents the dominant structure, with or without associated alteration, veins, and secondary porosity, and (iii) altered granites. The altered granites were further subdivided into three subtypes: (a) altered-replaced granites, defined by extensive mineral re-equilibration textures, including pseudomorphic replacement of plagioclase by epidote and biotite to chlorite; (b) altered-cemented granites, marked by intergrowths and precipitation of fine-grained secondary minerals, including albite, epidote, chlorite, calcite, quartz, and pyroxene, which cement the rock matrix; and (c) altered-porous granites, characterized by abundant secondary porosity resulting from mineral dissolution and leaching of biotite, felspar, and quartz, along extensive precipitation of secondary albite and quartz (Figures 3-9). Additionally, fractured rocks locally exhibit closely spaced fracture networks that extend over several tens of centimeters to meters, corresponding to the high-density fracture zones (HDFZ) described in the first part of this work (Nordbäck et al., 2026).



241

242 **Figure 3**: Representative rock samples from the Vehmaa Rapakivi Batholith. (a) Typical massive and unaltered
243 medium-grained granite (sample KUS-045). (b) View of a fractured granite perpendicular to a fault plane (sample
244 KUS-036) showing closely spaced fractures transecting a rapakivi granite. (c) View perpendicular to a fractured
245 granite (sample KUS-050), illustrating a closed-spaced, high density fracture zone (HDFZ). (d–f) Examples of altered
246 granite showing contrasting textural and mineralogical characteristics: (d) highly porous granite with pervasive
247 secondary voids related to mineral dissolution; Densely cemented granite characterized by a fine-grained matrix
248 intergrowth of feldspar (Fel), plagioclase (Pl), quartz (Qz), calcite (Cal), and pyroxene (Px), associated with K-feldspar
249 replacement by REE-enriched epidote (REE-Ep); (f) granite showing extensive replacement of plagioclase by epidote.
250 Other mineral abbreviations are: Bio = biotite, Chl = chlorite, Ep = epidote, Mcr = microcracks.

251

Massive granite

The massive, weakly altered granite (Figures 3a and 4) display a medium- to coarse-grained, equigranular to locally porphyritic texture dominated by K-feldspar, plagioclase, quartz, and biotite. The massive granite contains accessory minerals, including fluorite, apatite, zircon, monazite, Ti oxides such as ilmenite and rutile, as well as minor topaz and pyrite, typically occurring as disseminated grains or inclusions within biotite and feldspars (Figures 4a, f). Overall, the granite exhibits a compact, interlocking crystalline fabric with sharp crystal boundaries and negligible porosity, consistent with a largely unmodified rapakivi granite. Only few, isolated micropores are present, typically occurring adjacent to altered minerals (Figures 4b, f). In detail, biotite commonly hosts abundant zircon, monazite, and apatite inclusions, in which zircon and monazite are typically surrounded by well-developed pleochroic halos (Figure 4c). Contrasting, fluorite and minor topaz occur mainly as interstitial minerals and/or along cleavage planes within plagioclase (Figure 4e). Alteration is weak and spatially restricted with plagioclase that shows incipient sericitization along cleavage planes and grain margins, whereas biotite undergoes minor replacement by chlorite (Figure 4c).

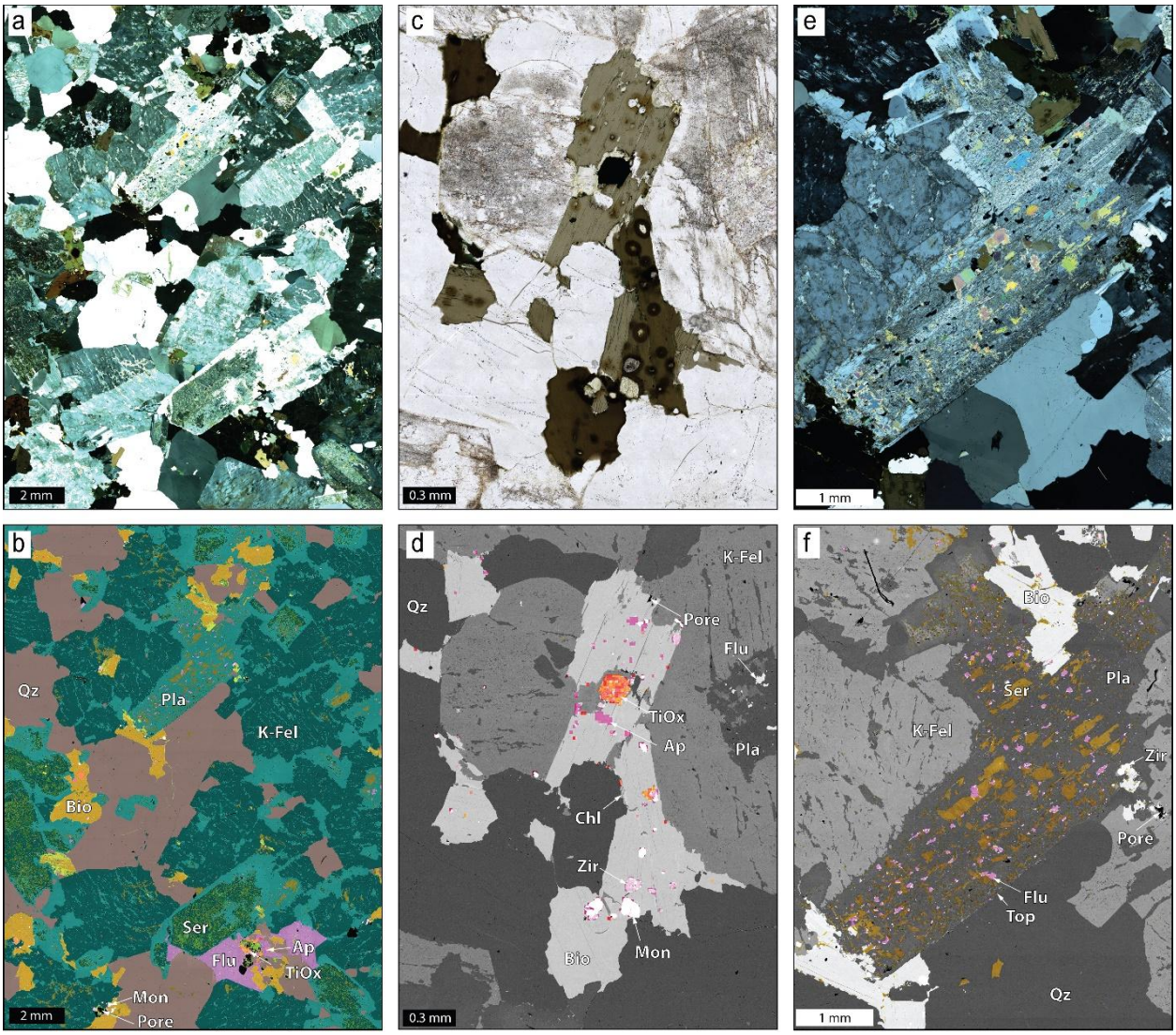


Figure 4: Thin-section and SEM mineral-mapping characterization of the massive, weakly altered granite, sample KUS-045. (a) Cross-polarized light image and (b) corresponding SEM mineral map showing an interlocking mosaic of K-feldspar (K-Fel), plagioclase (Pl), quartz (Qz), and biotite (Bio), with accessory fluorite (Flu), apatite (Ap), Ti-oxides (TiOx), monazite (Mon), and minor sericite (Ser). Close-up images of a biotite grain in plane-polarized light (c) and backscattered-electron mode (d) showing abundant zircon (Zir) and monazite (Mon) inclusions surrounded by pleochroic halos, together with apatite (Ap) inclusions. Feldspars adjacent to the biotite show weak sericitization along cleavage planes. Cross-polarized light (e) and backscattered-electron images (f) show a plagioclase grain partially replaced by sericite (Ser), abundant fluorite (Flu) inclusions, and minor topaz (Top) along cleavage domains.

Fractured granite

In the fractured facies (Figure 3b, c, 5, and 6), primary magmatic minerals remain recognizable but are transected by a dense network of microfractures and veinlets up to 1 cm-wide). The fractures display variable aperture and continuity, usually in the millimeter range, from open microcracks to fully sealed veins, cutting across minerals or following crystal boundaries and cleavage planes (Figures 5 and 6), and in places forming zones of incipient cataclasis where minerals are intensely fractured, displaced, or rotated (Figure 6e). Fracture density is highly variable across the samples, with some domains displaying closely spaced, subparallel sets (Figure 6), and others forming polygonal, anastomosing, or branching networks. The principal fractures are broadly planar and up to five millimeters wide, with narrower subsidiary sets branching outward into the surrounding rock matrix (Figure 5a, e). In some locations, the fracture network becomes markedly interconnected, forming multi-directional structures that correspond to the high-density fracture zone (HDFZ) described in the first part of this study (Figures 3c and 6a, b; Nordbäck et al., 2026). X-ray tomography and mineral mapping reveal that these HDFZs define a well-connected micropore system, with microcracks and dissolution pores reaching 8% porosity and 74% connectivity at an 11µm XCT resolution (Figure 6c).

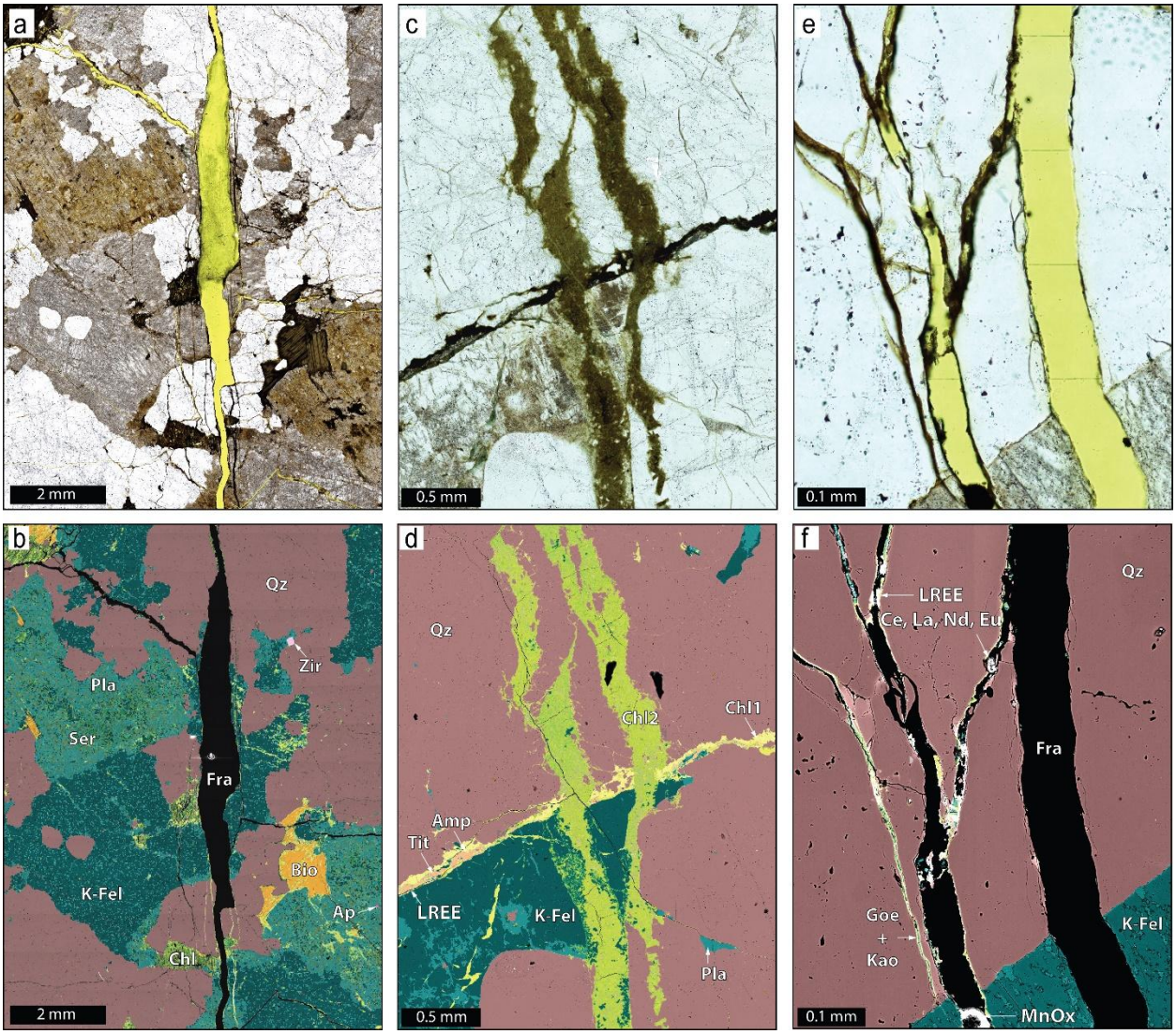


Figure 5: Thin-section and mineral-mapping characterization of fractured granite from samples KUS-004 (a, b, e, f) and KUS-060 (c, d). (a) Plane-polarized light image and (b) corresponding SEM mineral map of an open fracture cutting a rapakivi granite composed of K-feldspar (K-Fel), plagioclase (Pla), quartz (Qz), and biotite (Bio), with accessory apatite (Ap) and zircon (Zir), and minor sericite (Ser) and chlorite (Chl) alteration phases mainly localized adjacent to fracture walls. (c) Plane-polarized light image and (d) corresponding SEM mineral map showing two generations of chlorite-rich veins, distinguished by their cross-cutting relationships. The first generation (Chl1) is associated with abundant titanite (Tit), Fe-Ca-rich amphibole (Amp) and LREE enrichment, including Ce, La, Nd, and Eu, whereas the second generation (Chl2) is dominated by chamosite, an Fe-rich chlorite typical of hydrothermal alteration. (e) Plane-polarized light image and (f) corresponding SEM mineral map of a branching network of partially open microfractures, in which dark fracture-wall coatings are associated with goethite (Goe), kaolinite (Kao), Mn-oxide (MnOx), and LREE enrichment, including Ce, La, Nd, and Eu, along fracture margins.

Within the fractures, chlorite, epidote, quartz, titanite, fluorite, pyroxene, amphibole, goethite, and kaolinite occur as fine-grained elongate bands to patchy masses (Figures 3b, 5, and 6). In detail, chlorite is the most common fracture-related mineral, occurring consistently within both NW-and NE-trending strike-slip faults, forming well-developed veins that crosscut each other and the surrounding host rock fabric (Figure 5c). XRD and SEM–EDS analyses indicate that the chlorite is dominated by chamosite, an Fe-rich variety commonly associated with hydrothermal activity and propylitization (Inoue et al., 2010; Supplementary Material). Epidote more commonly replace plagioclase, but is also present along the fractures as discrete patches and vein-parallel aggregates (Figure 7a, b). Quartz veins are less common. Where present, they display a dense multidirectional and interconnected network that crosscuts all primary and secondary mineral phases (Figure 7a). Titanite and fluorite also occur as scattered, small crystals concentrated within fracture interiors and along narrow subsidiary veins (Figures 5d and 7a, b).

Pyroxene veins were identified in two locations (site AUV1, and at the Vuosnainen cross-section; Figure 1 and 2), all consistently within NW trending strike-slip faults. In outcrop, these pyroxene veins occur as discrete, well-defined bands up to 1 cm wide that sharply crosscut the host rock fabric. The veins are typically surrounded by well-developed alteration halos extending up to 50 cm in both directions from the veins (Figure 2), whereas in thin section they show more diffuse contacts with the surrounding quartz–feldspar assemblage (Figure 6b). XRD and SEM–EDS analyses indicate that the pyroxene belongs to the Na–Fe-rich aegirine–augite series (Supplementary Material). Similar mafic veins occur within strike-slip faults at sample locations KUS-009 and KUS-060 (Figure 1), but they are composed mainly of Fe–Ca-rich amphibole, chlorite, and titanite (Figure 5c). Goethite and kaolinite also occur as fine-grained materials that

typically form discontinuous to regular films along fracture walls or lining the propylitic assemblage (Figure 5e and 6a).

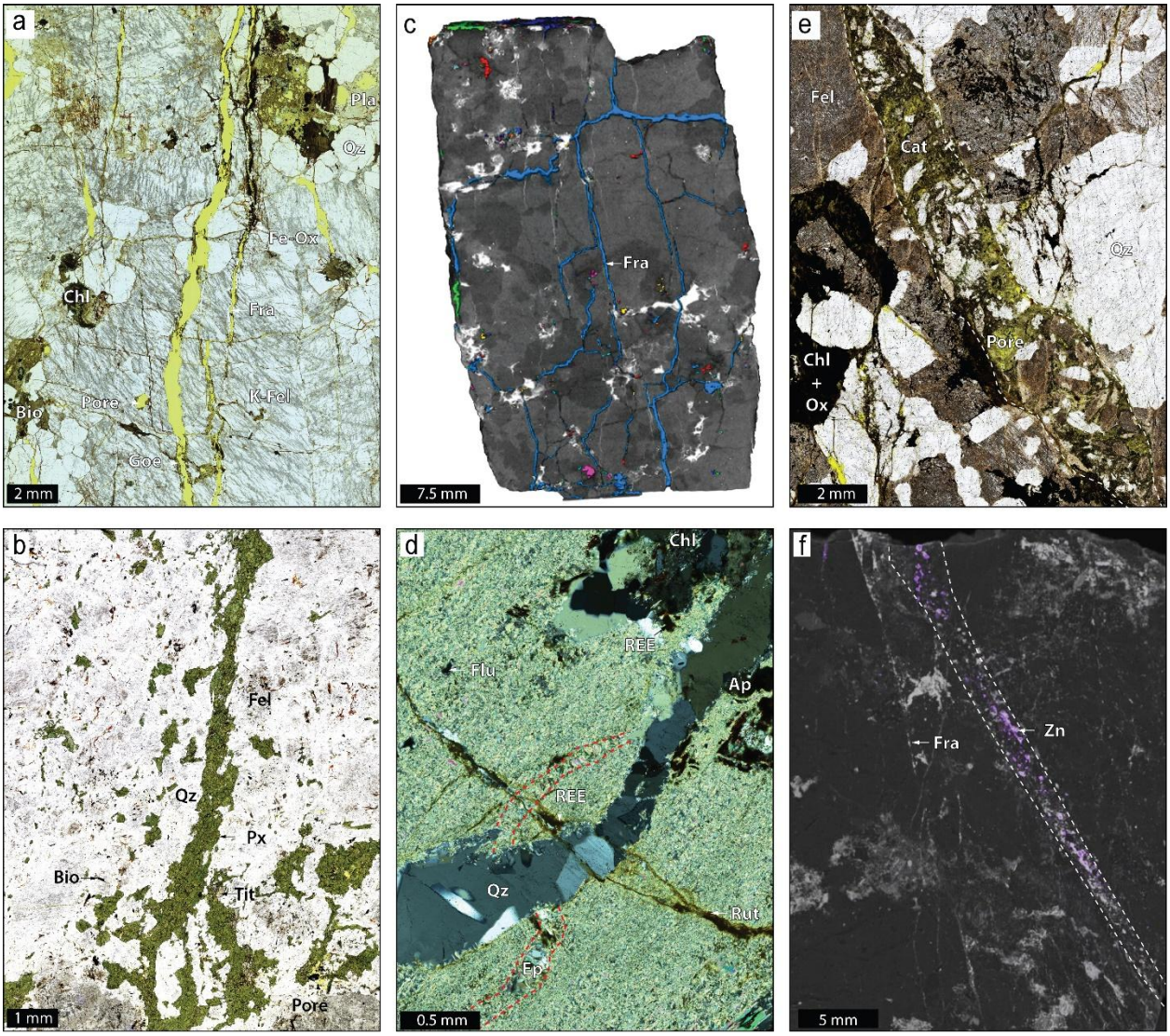


Figure 6: (a) Plane-polarized light image showing a densely fractured granite composed mainly of K-feldspar (K-Fel), plagioclase (Pla), quartz (Qz), and biotite (Bio), with chlorite (Chl), Fe-oxide (Fe-Ox), goethite (Goe), and secondary pore space developed along fractures, representative from the high-density fracture zone (HDFZ). (b) Plane-polarized light image showing an aegirine–augite pyroxene (Px) veins cutting the granite. (c) X-ray computed tomography (X-CT) overview image representative from the HDFZ acquired at 24.5 µm resolution, showing a dense, open, and well-connected fracture network (Fra) cutting the granite. (d) Cross-polarized light image showing quartz (Qz)- and epidote (Ep) veins associated with fluorite (Flu), rutile (Rut), and REE-enriched domains. (e) Plane-polarized light image showing a cataclastic zone with fragmented quartz and feldspar grains, chlorite (Chl), and secondary pore space. (f) Elemental distribution map highlighting Zn-rich veinlets within fractured and cataclastic zones.

Additionally, REE, including Ce, La, Nd, and Eu, as well as less common Mn-, Zn- and Cu-bearing phases locally occur as discrete fracture-filling materials. Within the fractures, REE occurs in two main textural relationships: (i) fine-grained material associated with or lining chlorite, epidote, goethite, and kaolinite (Figures 5d, f) and (ii) concentric Mn–REE-rich nodules (Figures 5f). Zn-, Pb-, and Cu-bearing phases were only identified at Vuosnainen (location AUV1 in Figure 1), within a major NW-trending strike-slip fault zone, and in association with replaced and cemented granites (Figure 6f, 8, and 9), as describe in the following sections.

Altered-replaced granite

The altered-replaced granite (Figures 3f and 7) displays extensive textural reorganization resulting from mineral replacement, consistently occurring in association with strike-slip faults. At the thin-section scale, this rock facies is characterized by pervasive pseudomorphic replacement of feldspar and biotite by epidote, chlorite, and sericite (Figures 7a). In detail, plagioclase, and less commonly K-feldspar, are partially to completely replaced by microcrystalline aggregates of sericite and REE-rich epidote, whereas biotite is completely replaced by chlorite and, less often, by muscovite. XRD analysis indicates that the sericite includes phengite–ferroceladonite–celadonite varieties, confirming the presence of fine-grained K-bearing phyllosilicate alteration phases (Supplementary Material). Altered biotite and chlorite are also often associated with oxides, including rutile and ilmenite (Figure 7b, and 9e).

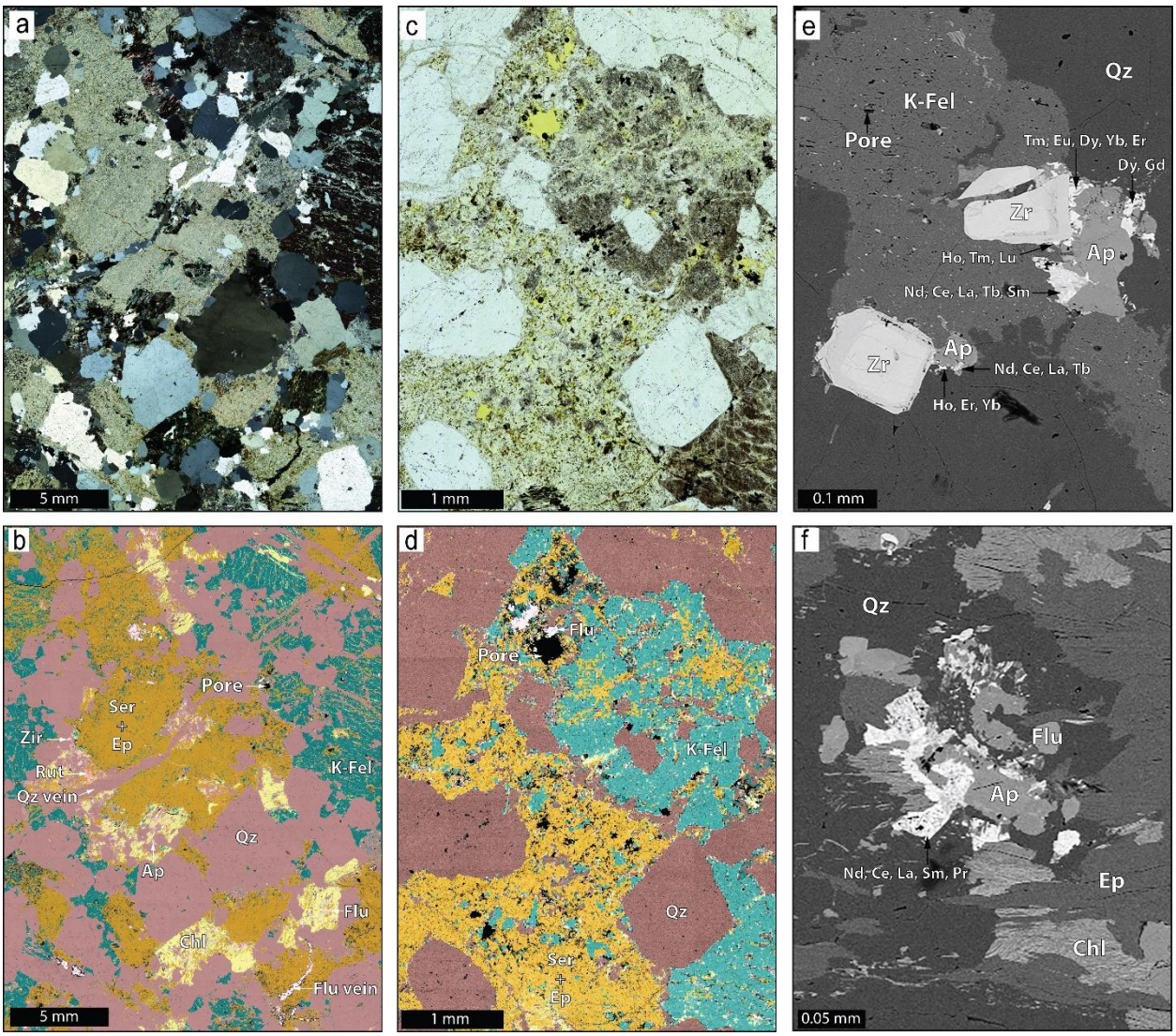


Figure 7: Characterization of an altered-replaced granite (sample KUS-016). (a) Cross-polarized light image showing an altered granite composed mainly of quartz (Qz), K-feldspar (K-Fel), and biotite and plagioclase relics, overprinted by pervasive replacement of plagioclase by sericite, epidote (Ser + Ep), and fluorite (Flu), and biotite replaced by chlorite (Chl), fluorite, and rutile (Rut). The sample also preserves remnants of primary accessory minerals, including apatite (Ap) and zircon (Zir), together with pervasive quartz veining, localized fluorite veins, and secondary microporosity developed due to partial leaching of biotite and plagioclase. (b) Corresponding SEM–EDS mineral map as shown in (a). (c) Plane-polarized light image showing a detail of an altered feldspar-rich domain with pervasive sericite–epidote replacement, localized fluorite precipitation, and secondary microporosity associated with partial dissolution of K-feldspar and plagioclase. (d) Corresponding SEM mineral map as in (c). (e) Backscattered-electron image showing zircon (Zr) and apatite (Ap) grains surrounded by REE along accessory-mineral reaction margins. (f) Backscattered-electron image showing an apatite–fluorite-bearing alteration domain associated with epidote (Ep) and chlorite (Chl), where discrete LREE-rich material occurs along mineral contacts and reaction domains.

Occasionally, REE-rich precipitates occur as isolated crystals around zircon, apatite, and fluorite, as shown by the bright domains in the backscattered-electron images (Figures 7e, f). These crystals form fibrous to irregular patches of fine-grained material along mineral margins and reaction borders; however, the exact mineral of these REE-rich phases remains uncertain. Possible candidates include secondary monazite, rhabdophane (a hydrated rare-earth phosphate), REE-rich apatite, or REE fluorocarbonates like bastnäsite and synchysite, which confirmation would require targeted analysis such as Raman spectroscopy. Within this rock facies, HREE are preferentially associated with zircon whereas LREE concentrated around apatite and within apatite–fluorite-bearing reaction zones (Figures 7e, f).

Throughout the altered-replaced granite, secondary microporosity is often observed where felspar is replaced by microcrystalline sericite–epidote aggregates, whereas fractures are largely filled by quartz and fluorite veins (Figure 7a, b). These micropores occur as irregularly-shaped, scattered voids, typically around 30 μm and locally up to 500 μm in diameter. They are commonly distributed along mineral cleavage and boundaries, producing a patchy to sieve texture mainly within the altered feldspar framework and secondarily within biotite domains.

Altered-cemented granite

The altered-cemented granite is characterized by a dense and compact crystalline fabric dominated by extensive intergrowth of fine-grained minerals (Figures 3e and 8), always occurring within strike-slip faults or in association with multiple clinopyroxene veins (Figure 2). The original granitic texture is largely to completely obscured by a secondary mineral assemblage dominated by albite, K-feldspar, epidote, quartz, calcite, and two compositionally distinct Ca–Fe- and Mg–Fe-rich silicates, accompanied by local biotite, chlorite, apatite, fluorite, titanite, zircon, sphalerite,

394 galena, Fe–Ti oxides, and minor goethite. Only few isolated vugs remain, typically small (<50
395 μm), rounded cavities bordered by epidote–chlorite or Fe-oxide aggregates. In detail, the
396 compositionally distinct Ca–Fe- and Mg–Fe-rich silicates occur as globular- to irregularly-shaped
397 aggregates scattered throughout the rock mass (Figures 8c, d). The Ca–Fe-rich phase is
398 provisionally classified as a pyroxene/pyroxenoid-like mineral, whereas the Mg–Fe-rich phase is
399 compositionally consistent with the enstatite–ferrosilite pyroxene series. For simplicity, these
400 minerals are collectively referred to here as pyroxenes, and more thorough analysis is required for
401 precise identification. Albite and K-feldspar occur as irregular domains embedded within the fine-
402 grained cemented assemblage, commonly showing diffuse margins and close intergrowths with
403 quartz, epidote, calcite, chlorite, and pyroxene (Figures 8d). Epidote is one of the principal
404 constituents, occurring as fine- to coarse-grained irregularly-shaped aggregates that commonly
405 contain REE-enriched zones in EDS maps and are intergrown with fine-grained pyroxene,
406 feldspar, quartz, and calcite (Figures 8c, e). Calcite mainly occurs as blocky to irregularly-shaped
407 crystals intergrown with the surrounding minerals, locally forming cemented domains (Figure 8d).
408 Fluorite occurs as scattered fine-grained material usually together with apatite and zircon (Figure
409 8d). Biotite is preserved as scattered relicts, partly or totally replaced by chlorite and often
410 associated with titanite, apatite, or oxides, whereas sericite occurs pervasively along feldspar
411 crystals (Figures 8e, f). Sphalerite and galena form fine-grained, localized aggregates intergrown
412 with calcite, pyroxene, fluorite, and REE-rich epidote (Figures 8c, d).

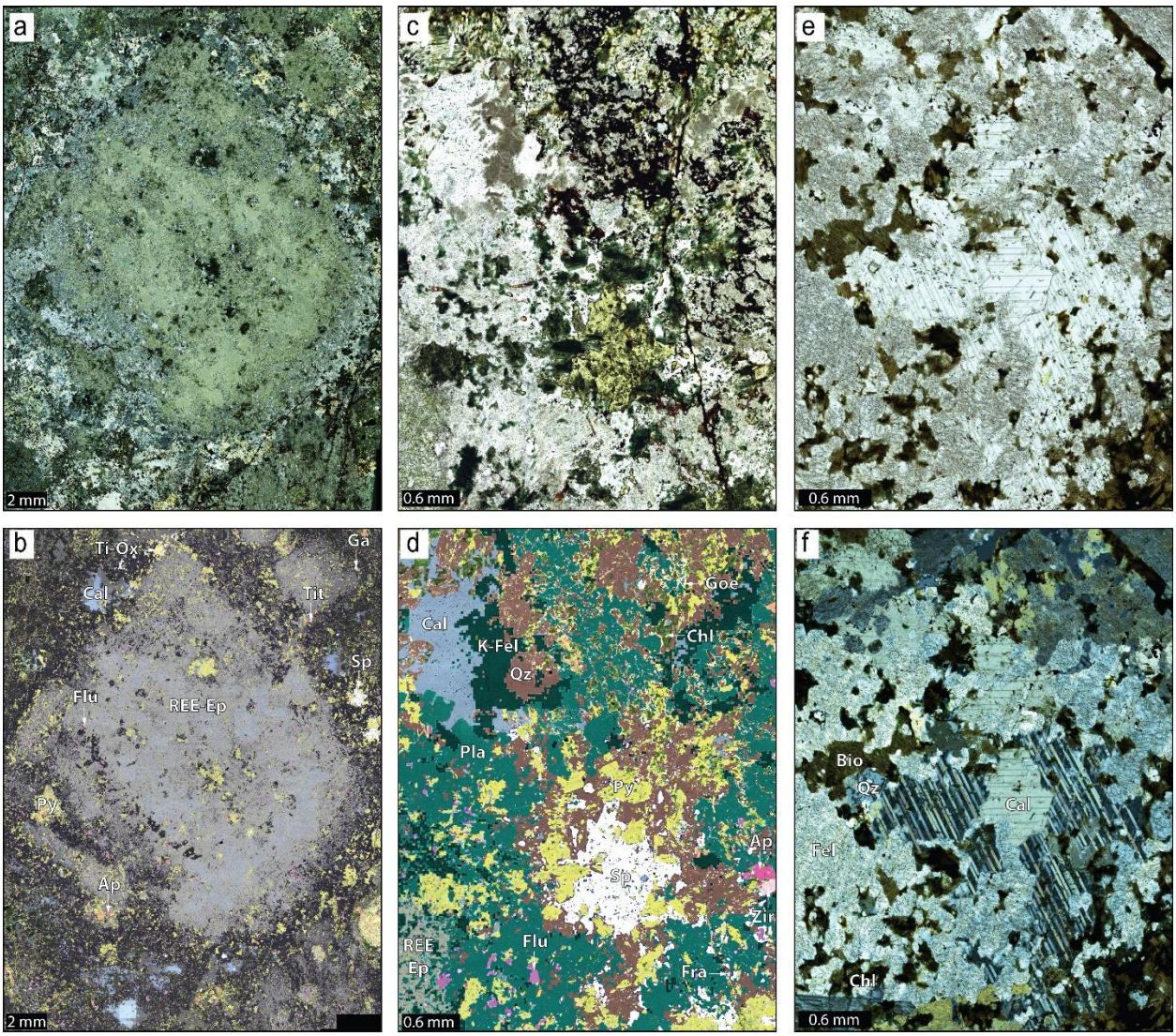


Figure 8: Thin-section and mineral-map images of the altered-cemented granite. (a) Cross-polarized light image and (b) corresponding SEM–EDS mineral map showing a densely cemented and replaced rock dominated by a fine-grained intergrowth of feldspar, quartz, Fe-rich pyroxene (Px), REE-rich epidote (REE-Ep), and calcite (Cal). Fluorite (Flu), apatite (Ap), titanite (Tit), Ti-oxide (Ti-Ox), galena (Ga), and sphalerite (Sp) are also present. (c) Plane-polarized light close-up and (d) corresponding SEM–EDS mineral map showing a highly cemented domain composed of fine-grained K-feldspar (K-Fel), plagioclase (Pla), quartz (Qz), Fe-rich pyroxene, REE-rich epidote, and calcite intergrown with sphalerite, fluorite, apatite, zircon (Zir), chlorite (Chl), and goethite (Goe) infilling cracks. (e–f) Plane- and cross-polarized light images showing calcite-rich cement filling former pores and intergrown with quartz, biotite, chlorite, and feldspar, documenting pervasive cementation and sealing of former pore spaces and fractures.

Altered-porous granite

The altered-porous granite is characterized by abundant secondary porosity developed through mineral dissolution, together with a partially preserved granitic framework overprinted by pervasive mineral replacement and recrystallization. This rock facies is composed mainly of albite, K-feldspar, chlorite, and quartz, with subordinate apatite, titanite, zircon, fluorite, and oxides (Figures 3d and 9). In detail, large feldspar crystals commonly preserve their primary morphology despite strongly corroded and irregularly-shaped margins, with K-feldspar extensively replaced by fine-grained albite, recording substantial albitization (Figure 9b). Locally, albite and quartz, accompanied by apatite, form fine-grained, mosaic-like aggregates of euhedral to subhedral crystals along pore margins, suggesting secondary precipitation and partial occlusion of pre-existing pore spaces (Figure 9b). Chlorite is pervasive, commonly forming fine-grained aggregates intergrown with albite and quartz, and locally lining pore margins or occupying interstitial spaces between feldspars. Chlorite is also locally replaced by fine-grained oxides, particularly rutile, along grain margins and alteration fronts (Figure 9b, e). Biotite is absent and was likely completely replaced by chlorite or removed by dissolution, whereas feldspar locally show partial leaching, collectively recording pervasive propylitic alteration of the original granitic fabric (e.g., Nishimoto and Yoshida, 2010; Sanchez-Alfaro et al., 2016).

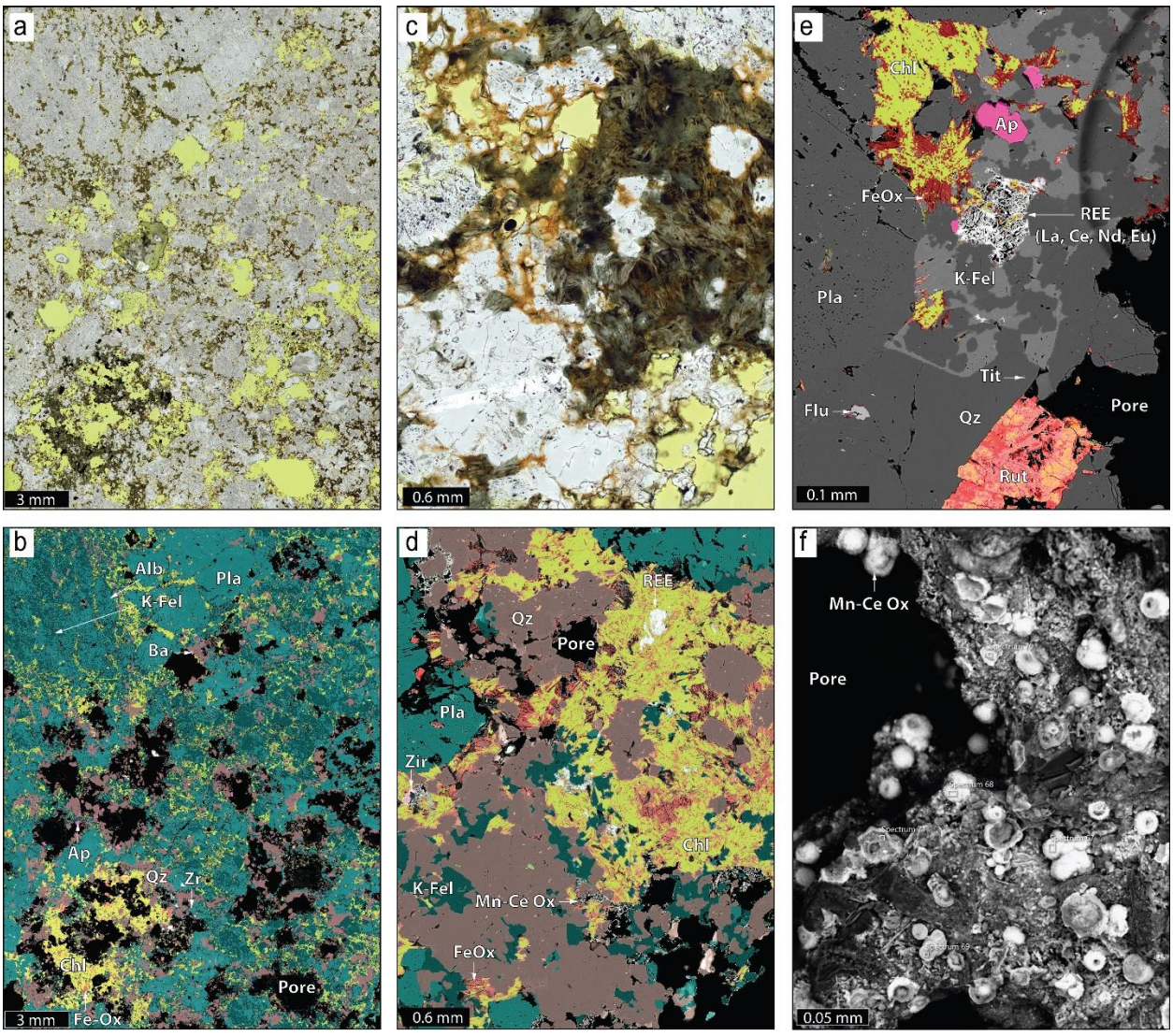


Figure 9: Thin-section and mineral-map characterization of the altered porous granite. (a) Plane-polarized light image and (b) corresponding SEM–EDS mineral map showing a strongly altered granite with abundant secondary porosity, replacement of biotite by chlorite (Chl) and K-feldspar to albite (Alb). Accessory minerals include zircon (Zr) and apatite (Ap), and barite (Ba) developed along pore walls. (c) Plane-polarized light close-up and (d) corresponding SEM–EDS mineral map showing a strongly altered domain in which biotite is replaced by chlorite and dark Fe-rich alteration products, forming irregular replacement textures. REE are concentrated along replacement fronts, whereas Mn–Ce–Fe-rich nodules occur along pore walls. (e) Backscattered-electron image showing chlorite, Fe-oxides (FeOx), apatite, titanite (Tit), rutile (Rut), fluorite (Flu), plagioclase (Pla), K-feldspar (K-Fel), quartz (Qz), and pore space. REE-enriched material, including La, Ce, Nd, and Eu, occurs along the margins of altered chlorite–Fe-rich domains and adjacent reaction borders. (f) High-magnification backscattered-electron image showing rounded Mn–Ce oxide nodules and Fe–Mn-rich material developed along pore walls.

453 REE-enriched material, including La, Ce, Nd, and Eu, is extensively deposited along pore walls
454 and commonly concentrated within chlorite-rich alteration domains associated with Fe–Ti oxides
455 and, locally, barite (Figure 9a, d, e). At higher magnification, pore walls are coated by abundant
456 rounded to concentric Fe–Mn–Ce-rich nodules (Figure 9f). The pore network of this lithofacies is
457 highly heterogeneous, ranging from isolated intracrystalline voids to patchy and locally coalescent
458 vugs up to 3 mm in diameter, with larger cavities and microporosity locally connected by narrow
459 pore throats and microfractures (Figure 9b, c).

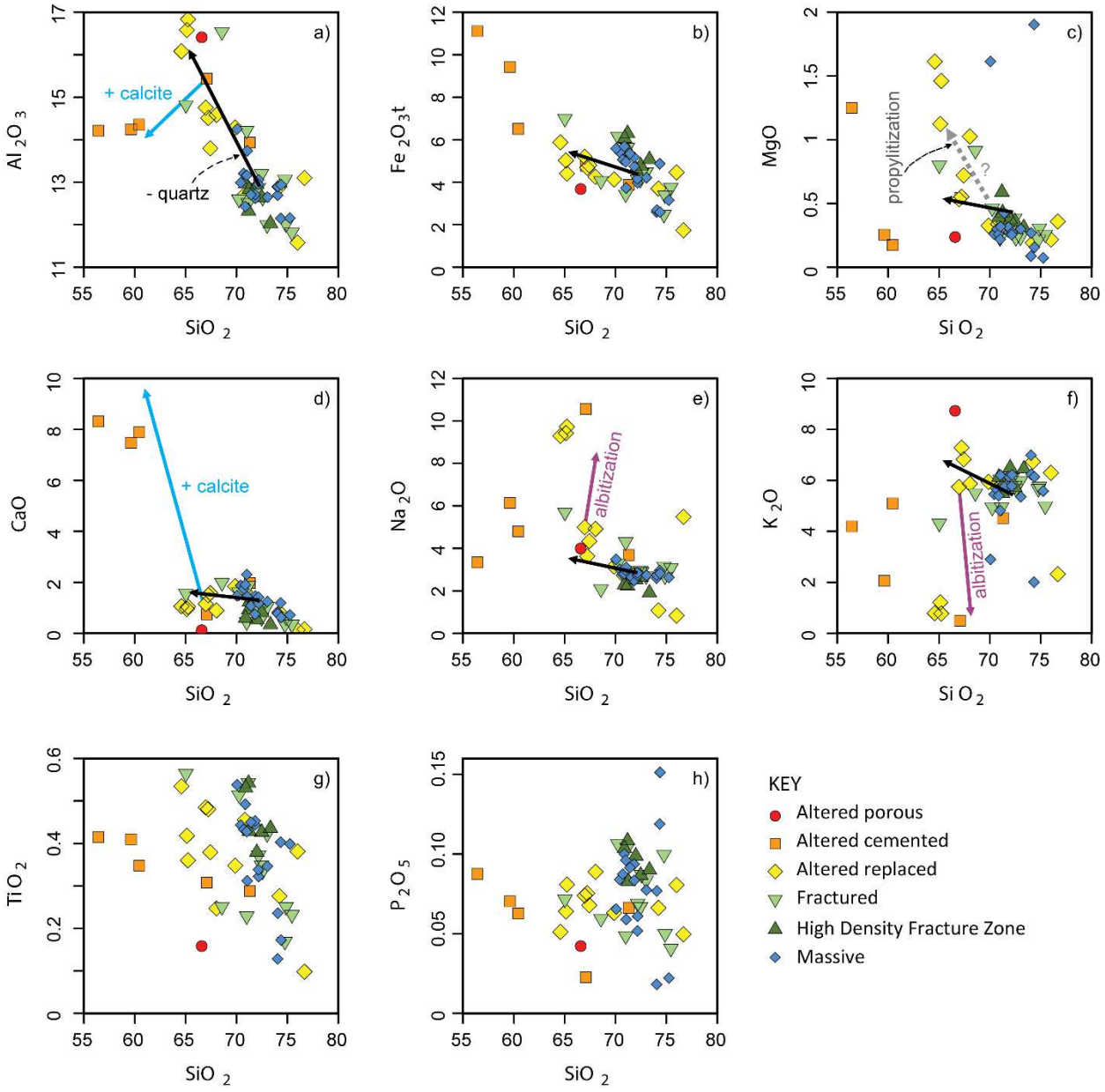
460 ## 5.2 Bulk Geochemistry

461 **Major and minor elements and loss-on-ignition (LOI)**

462 The bulk major and minor element concentrations of the different granitic groups are illustrated in
463 Figure 10 and full dataset (together with standard control) can be found in the Supplementary
464 Material. The massive granites are on average the most Si-rich and display rather homogeneous
465 composition across all analyzed samples (n=17), with outliers in MgO and K_2O contents only in
466 two samples. Conversely, altered-replaced granites are highly heterogeneous and typically show
467 an overall Al_2O_3, $Fe_2O_3^t$, MgO, and CaO contents increase while SiO_2 decreases, particularly in
468 the Vuosnainen area (area AUV1 in Figure 1). In this area, samples associated with both NW-and
469 NE-trending faults are substantially enriched in MgO while the silica is low compared to unaltered
470 samples, consistently with petrographic observations of propylitization (Figures 7-9). Four
471 samples exhibit relative Na_2O enrichment and K_2O depletion; three of these collected from the
472 core of the Vuosnainen fault zone and are discussed in more detail in the Geochemical Transect
473 section. Similarly, altered-cemented granites are also highly heterogeneous, from which three
474 samples show marked SiO_2 depletion, $Fe_2O_3^t$Fe enrichment, and substantial CaO increase

compared to massive granites. Additionally, one sample from the altered-cemented facies (KUS-035-A5) shows the lowest K_2O and the highest Na_2O content, consistent with petrographic evidence for albitization of K-feldspar near the faults (Figure 9b). The single altered-porous granite sample (KUS-006-A7) resembles the replaced facies but does not display MgO enrichment, which may reflect leaching of biotite and the absence of epidote and pyroxene, as seen in petrographic images (Figure 9).

Fractured granites exhibit trends comparable to those of altered-replaced, and massive granites; however, MgOMg enrichment and SiO_2 depletion are considerably less pronounced than in the former group. A few fractured samples show a slight decrease in K_2O with decreasing SiO_2, but most of the fractured samples are rather similar to the massive granites. TiO_2 and P_2O_5 show more scattered behavior than the major alkalis and Ca–Fe–Mg oxides, in which TiO_2 is locally elevated in altered samples. MnO only shows a marked enrichment in the altered-cemented granite relative to the other facies, although the wide range of values indicates strong intra-facies heterogeneity (Supplementary Material). LOI is generally low across most facies, but the altered-cemented granite shows the highest vales, consistent with localized precipitation of calcite and hydrous alteration minerals during carbonate-rich hydrothermal cementation (Supplementary Material).



491

492 Figure 10: Major and minor element plots versus SiO_2 for the five main lithological groups, with the number of
493 samples (N) indicated for each group: altered cemented granite (AC; N = 5), altered porous granite (AP; N = 1), altered
494 replaced granite (AR; N = 12), fractured granite (F; N = 13), high-density fractured zone granite (HDFZ; N = 6), and
495 massive granite (M; N = 17). All concentrations in wt.% and normalized to 100 wt.% volatile-free. The arrows have
496 been calculated as follows: "- quartz" (a-f) = -20 wt.% dissolution of quartz or dilution of SiO_2 from average M; "+
497 calcite" (a and d) = +10 wt.% of CaO to AC sample KUS-035-A5; “albitization” (e and f) = K-feldspar (~30 wt.% of
498 whole-rock) replaced by albite in AR sample KUS-021-A2; “propylitization” (c) = a first-order approximation of the
499 compositional changes associated with propylitic alteration.

500

Trace elements

Selected trace element bulk concentrations for the different lithological groups are presented as boxplots in Figure 11. Consistent with the major- and minor-element data, fractured granites show no systematic geochemical deviation from the massive granites. In contrast, the altered-porous granite is markedly enriched in many elements from the REE group, with a pronounced enrichment in light REEs (LREEs), particularly for La and Ce, in agreement with petrographic observations (Figure 9). Less pronounced LREE enrichment is observed in both altered-replaced and altered cemented granites.

The altered-cemented and altered-porous granites record the strongest trace-element modification, with localized enrichment in S, Sc, Sn, Zn, Cd, and Pb. In contrast, the altered-replaced granite shows only moderate Zn and S enrichment. Cu remains generally low to moderate across all lithofacies, with local increases only in fractured granites. Elevated S, Zn, Cd, and Pb concentrations in the cemented and porous facies are consistent with mineralogical observations of sphalerite and galena (Figures 6c and 8). Mineral maps further show that Sn is spatially associated with quartz-rich domains, whereas F contents are highly heterogeneous across the dataset, with localized high values in most lithofacies.

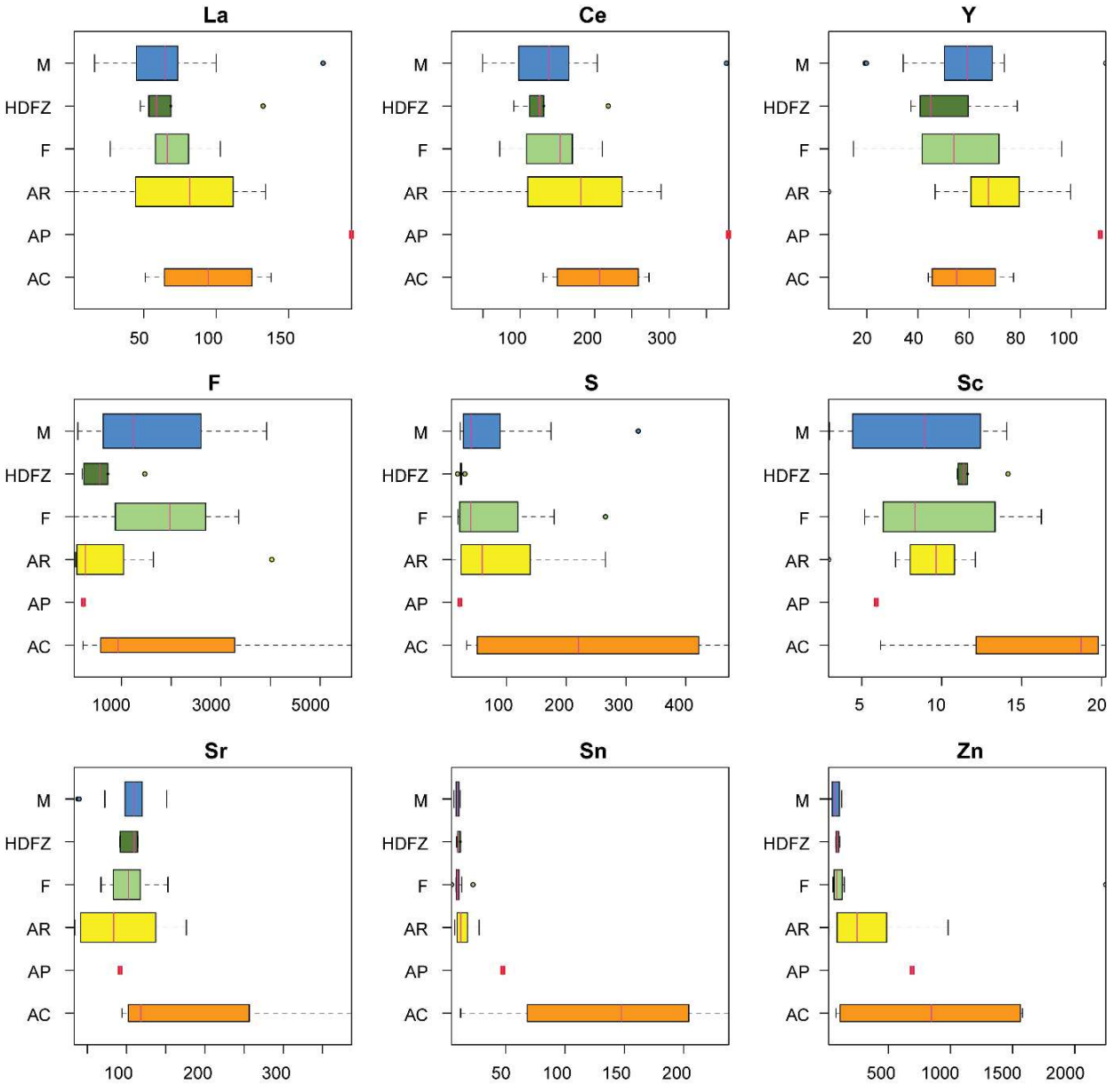


Figure 11: Boxplots of selected trace elements for the five main granitic facies, with the number of samples (N) indicated for each group: altered cemented granite (AC; N = 5), altered porous granite (AP; N = 1), altered replaced granite (AR; N = 12), fractured granite (F; N = 13), high-density fractured zone granite (HDFZ; N = 6), and massive granite (M; N = 17). All concentrations are reported in ppm. Boxes represent the interquartile range, the purple line indicates the median, and whiskers represent 24.65% of the distribution; outliers are shown as individual dot plots. Sn is of low accuracy (see Supplementary Material), but indicate a systematic increase in Sn abundance in the AP and AC groups relative to the other groups.

Geochemical transect across a strike-slip fault at Vuosnainen

Figure 12 illustrates the geochemical transect across a NW-trending strike-slip fault at Vuosnainen (AUV1 in Figure 1). The transect shows that whole-rock geochemical modification is strongly localized along the various fault strands. Samples collected from the host-block remain close to the massive granite average, whereas the fault core displays the strongest alteration signature, characterized by elevated Na_2O and MgO enrichment and marked K_2O depletion. CaO shows variable behavior, suggesting that Ca-bearing minerals such as epidote, calcite, fluorite, and pyroxene-like silicates are heterogeneously distributed within the fault zone. $Fe_2O_3^t$ and TiO_2 show more moderate variations, whereas P_2O_5 and F does not define a strong systematic trend. For trace elements, S, Sn, Zn, Pb, and REE concentrations substantially increases along the fault core and adjacent damage zones, consistent with petrographic evidence for sphalerite, galena, REE-bearing epidote, fluorite, and Sn-bearing microphases associated with quartz-rich domains in alike lithofacies.

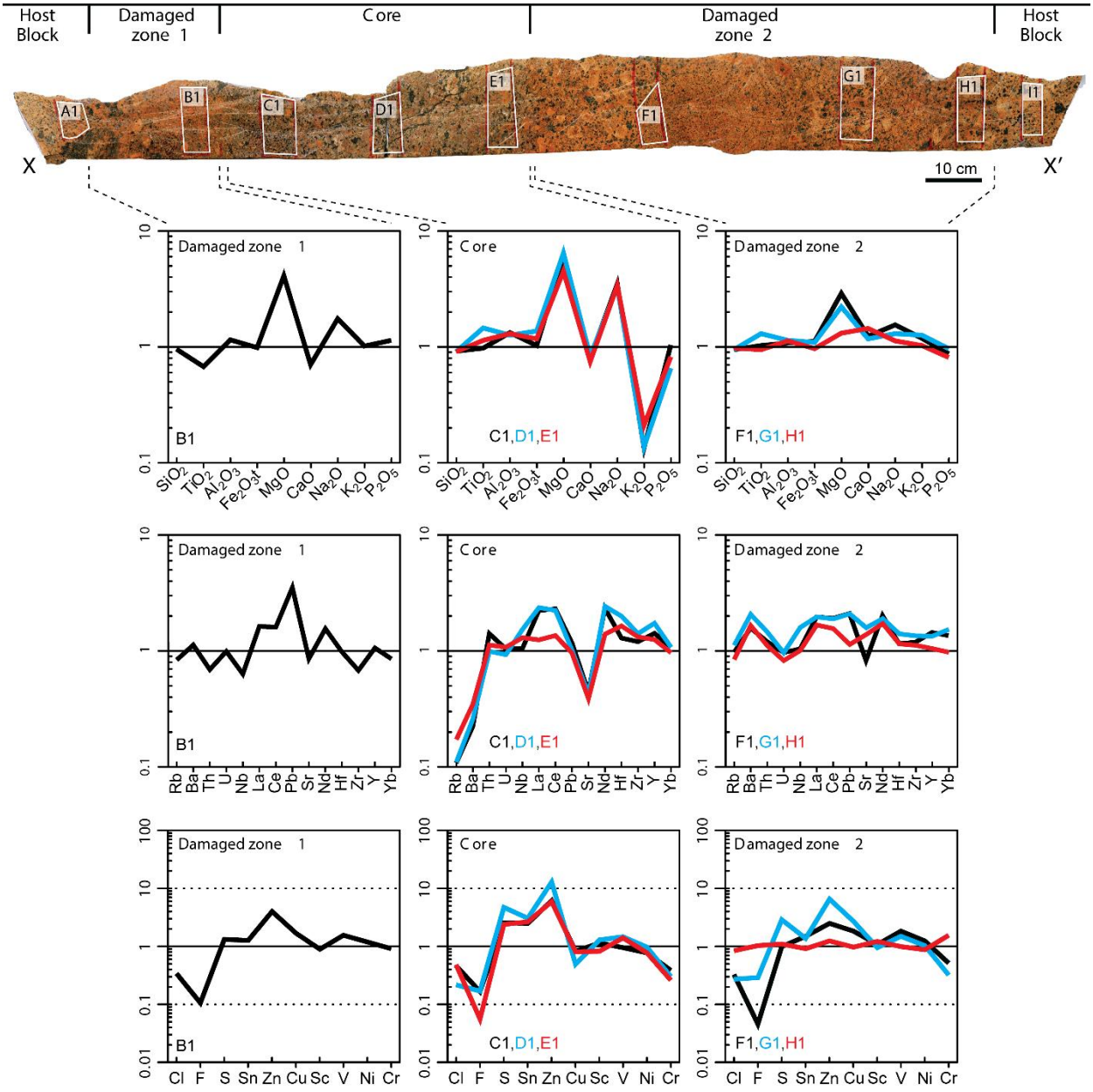
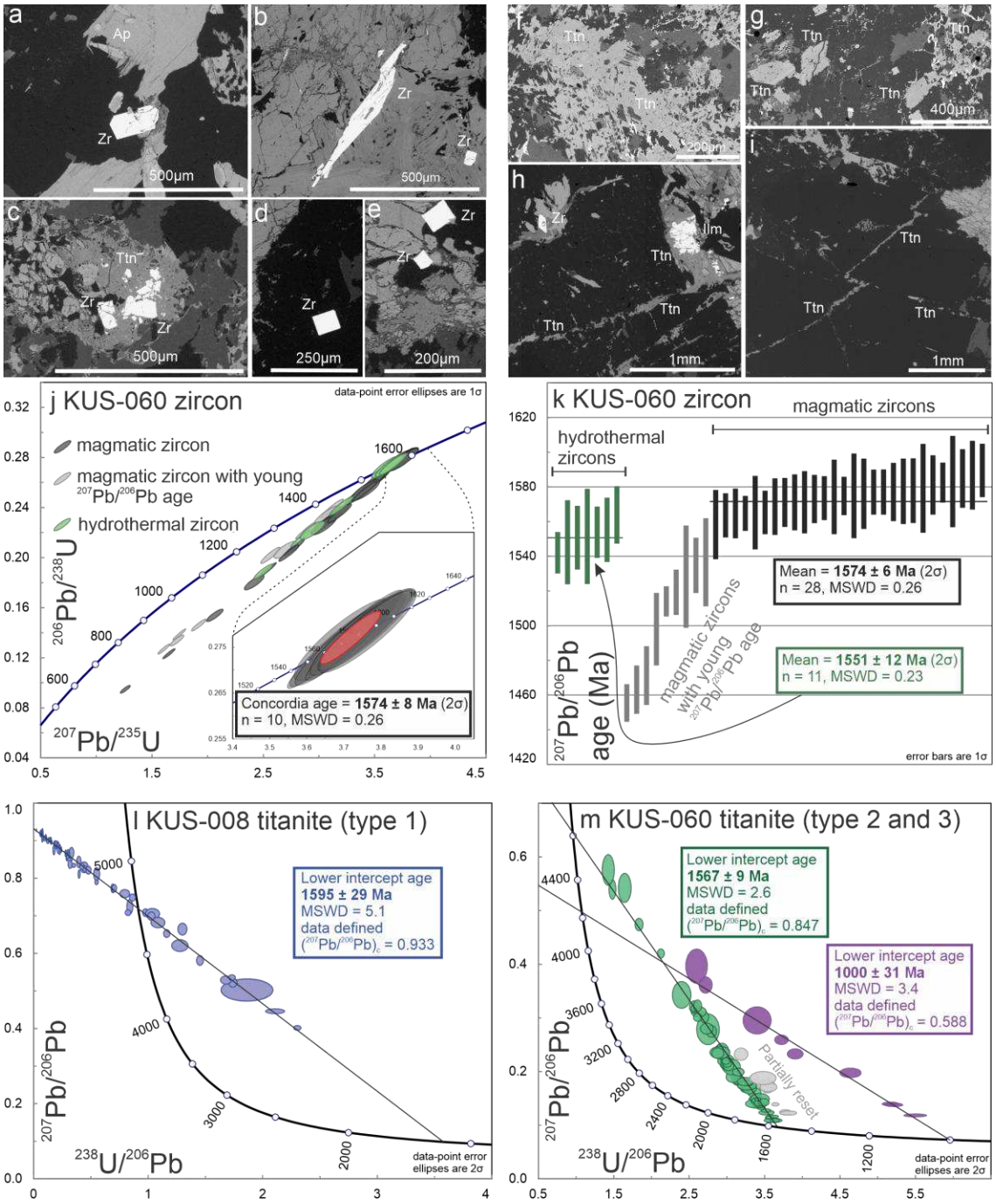


Figure 12: A cross-section through a strike-slip fault at the locality of Vuosnainen (sample series KUS-90, Figure 1). The multielement variation diagrams show major and minor element concentration (first row), incompatible trace elements (second row), and halogens, sulphur, and selected compatible trace elements (third row) across the architecture of the fault zone. All concentrations have been normalized to the average of the massive granite samples (n = 17) excluding notable outliers (n = 2). Letters A to I correspond to sample names. Both massive granite samples A1 and I1 only show deviations <15 % relative to the average massive granite and are thus not shown in the diagrams. Transect X–X′ is presented in Figure 2. Note that some of the elements shown here have lower analytical accuracy (marked in gray: Cl, F, S, Sc, Yb, Hf, Pb, Th, and U; see Supplementary Material); these elements are therefore used only for relative comparison among the sample groups.

5.3 Zircon and titanite U-Pb geochronology

Zircons were analyzed in sample KUS-060-A1 and titanites in samples KUS-060-A1 and KUS-008-A1, representing an amphibole–titanite–chlorite vein assemblage and the altered-cemented facies, respectively (Figures 5c and 8b). Zircons represent two textural types: prismatic grains typical of magmatic zircons (e.g., Corfu, 2003) and dipyramidal grains attributed to hydrothermal recrystallization (e.g., Yang et al., 2013). The size of the prismatic grains range between 50 and 600 µm along the c-axis and their morphology varies from stubby to large, elongated grains (Figure 13a and b). Prismatic grains are often broken and slightly dissolved but appear to lack clearly recrystallized parts (Figure 13c). The dipyramidal zircons are 30–50 µm in length appear as homogenous, square-like grains in BSE-images although a few grains with void spaces and inclusions are also present (Figure 13d and e).

Three textural types of titanite were distinguished. Type 1 occurs only in KUS-008-A1 as irregularly- shaped aggregates, formed after small euhedral titanite grains, which are associated with pyroxene, epidote, calcite ± ilmenite (Figure 13f and g). Type 2 replaces and commonly mantles ilmenite, whereas Type 3 forms thin veins and veinlets (Figure 13h and i). The distinction between Types 2 and 3 is not always clear because some Type 3 veinlets appear to originate from Type 2 titanite that mantle ilmenite. This textural transition from ilmenite to veinlet growth, together with the association of Type 1 with alteration minerals, indicates that all three titanite types are secondary products formed during successive stages of alteration.



568

569 Figure 13: representative zircon and titanite BSE-images and U-Pb data. a. prismatic igneous zircon, b. large,
570 elongated prismatic zircon, c. broken and possibly dissolved prismatic zircon, d. dipyramidal hydrothermal zircon, e.
571 two dipyramidal hydrothermal zircons, f. type 1 titanite aggregate, g. type 1 titanite aggregate resembling larger
572 prismatic titanite, h. type 2 titanite cluster surrounding ilmenite and type 3 titanite vein originating from the cluster, i.
573 type 3 titanite veins, j. all zircon U-Pb analyses on concordia diagram, k. all zircon analyses on $^{207}Pb/^{206}Pb$ age
574 diagram, l. type 1 titanite U-Pb analyses on Tera-Wasserburg diagram, m. type 2 and 3 titanite U-Pb data on Tera-
575 Wasserburg diagram.

In total, 50 spots on zircons were analyzed from the sample KUS-060-A1 (Figure 13j and k). Of these 37 spots were placed on prismatic zircons and 10 analyses plot on concordia curve yielding a concordia age of 1574 ± 8 Ma (2σ, n = 10, MSWD = 0.26). Most of the analyses are discordant, indicating Pb-loss, and by using all these analyses an upper intercept age of 1575 ± 7 Ma (2σ, n = 28, MSWD = 0.24) and a weighted average $^{207}Pb/^{206}Pb$ age of 1574 ± 6 Ma (2σ, n = 28, MSWD = 0.26) can be calculated. A subset (n = 10) of discordant analyses shows a decreasing trend in $^{207}Pb/^{206}Pb$ ages. These are attributed to Pb-loss coupled with common Pb, which has affected the $^{207}Pb/^{206}Pb$. Therefore, these analyses were omitted from age calculations. Seven analyses from the hydrothermal zircons show $^{207}Pb/^{206}Pb$ ages between 1564 and 1542 Ma with a weighted average $^{207}Pb/^{206}Pb$ age of 1551 ± 12 Ma (2σ, n = 7, MSWD = 0.23). Three of these analyses are concordant. Six analyses were rejected due to low analytical quality.

A total of 164 spots on titanites were analyzed from the two samples, including 66 on Type 1 titanite in KUS-008-A1. These analyses define a coherent array on the Tera–Wasserburg diagram and yield a lower-intercept age of 1595 ± 29 Ma (2σ; n = 66; MSWD = 5.1; modelled ($^{207}Pb/^{206}Pb$) c=0.933; Figure 13l). The U concentration of these titanites is extremely low (0.7-25 ppm) – this highlights the difference between type 1 and type 2 and 3 titanites – resulting in low radiogenic Pb composition and large portion of common Pb. Thus, the analyzes are mostly placed in the upper end of the mixing line between radiogenic and common Pb. However, the spread is large enough to define a linear array reflecting binary mixing between radiogenic and common Pb resulting in a reliable age estimate.

The remaining 98 analytical spots were placed on Type 2 and Type 3 titanite in sample KUS-060-A1, with no systematic difference in U–Pb age between the two textural types. Sixty-four analyses define a lower-intercept age of 1567 ± 9 Ma (2σ; n = 64; MSWD = 2.6; modelled ($^{207}Pb/^{206}Pb$)

599 c=0.847; Figure 13m). A younger population of nine analyses yields a lower-intercept age of 1000
600 ± 31 Ma (2σ; n = 9; MSWD = 3.4; modelled ($^{207}Pb/^{206}Pb$) c=0.588). A further nine analyses plot
601 between the 1568 and 1000 Ma arrays, suggesting partial isotopic resetting or mixed signatures.
602 Nine analyses were rejected due to poor analytical quality, including spots placed outside the target
603 grain or laser penetration through the grain.

604 5.4 Petrophysical Analysis

605 A total of 39 cylindrical cores representing the five petrographic facies of the Vehmaa Rapakivi
606 Batholith (i.e., massive, fractured, altered-porous, altered-replaced, and altered-cemented) were
607 analyzed for density, connected porosity, permeability, elastic wave velocities, electrical and
608 magnetic properties, thermal conductivity, and specific heat capacity (Figures 14 and 15;
609 Supplementary Material).

610 Density

611 Massive samples exhibit a narrow density range (2586–2673 kg m^{-3}), largely overlapping with
612 fractured samples (2637–2664 kg m^{-3}; Figure 14). Altered samples show the largest variability,
613 with altered-porous facies exhibiting the lowest densities (2273–2359 kg m^{-3}), altered-replaced
614 samples clustering at intermediate values (2593–2639 kg m^{-3}), and altered-cemented facies
615 reaching the highest densities in the dataset (2635–2828 kg m^{-3}).

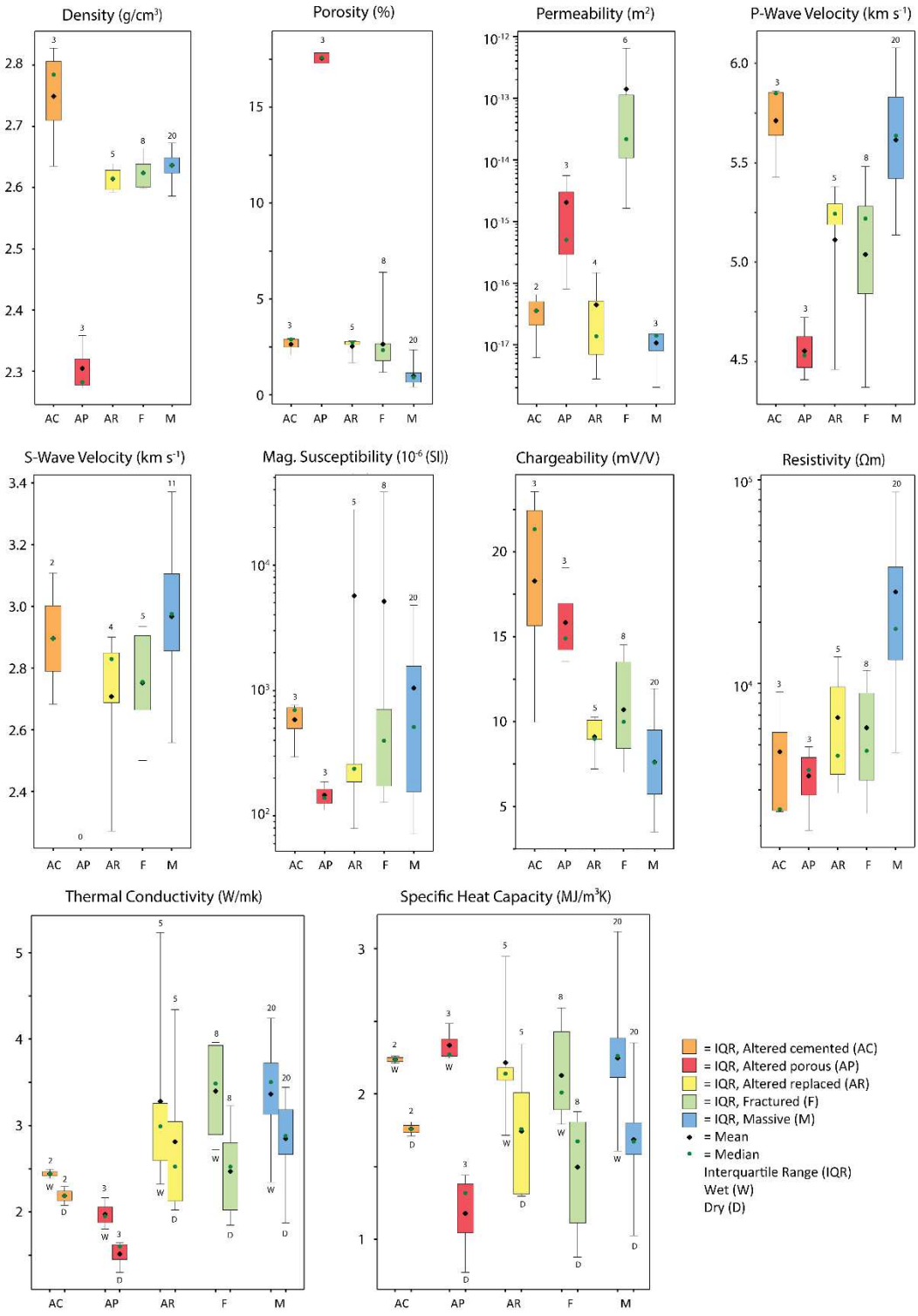


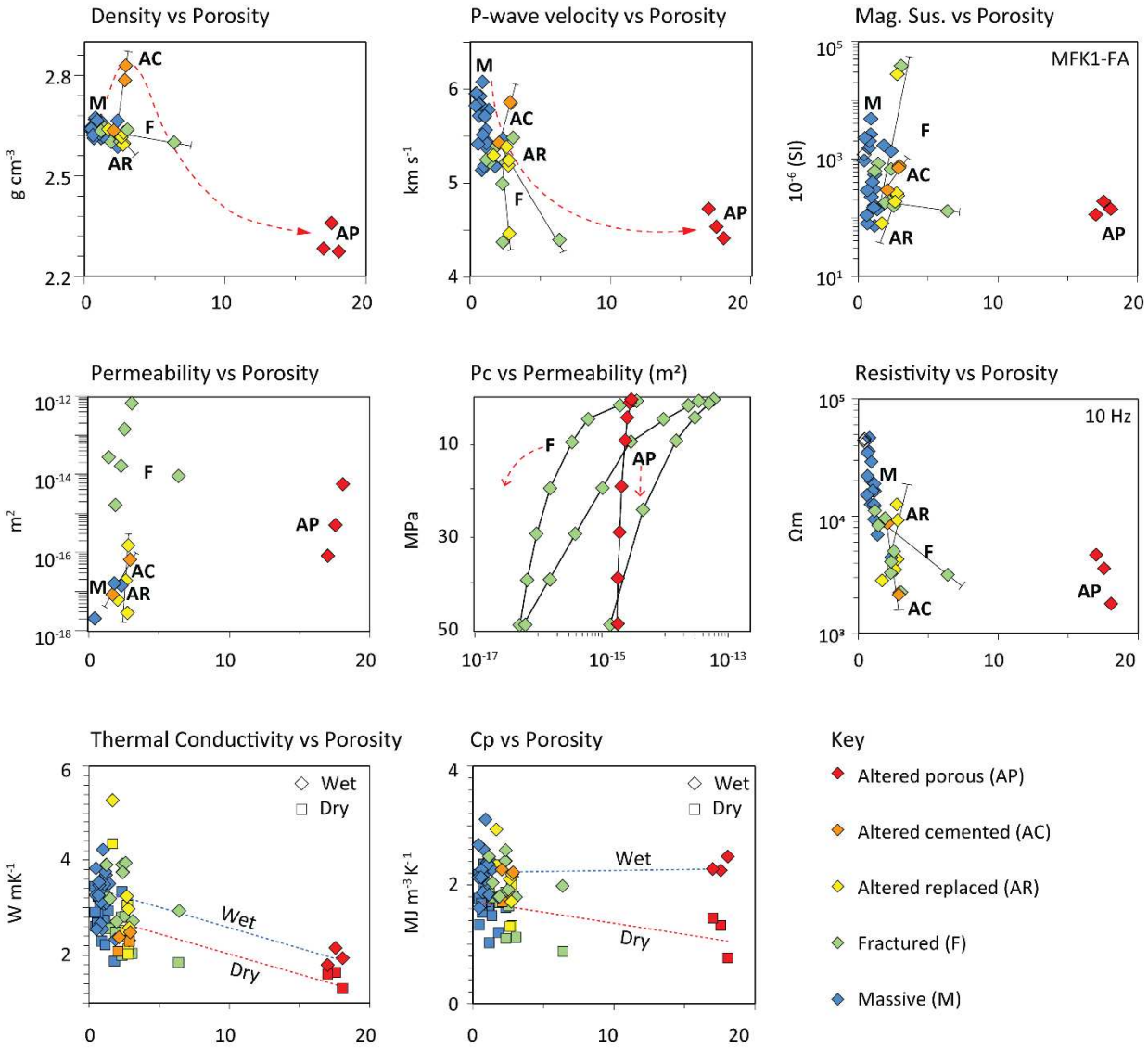
Figure 14: Boxplots showing the petrophysical variation for five lithological groups: altered cemented (AC), altered porous (AP), altered-replaced (AR), fractured (F), and massive (M). Boxes represent the interquartile range (IQR), with black dots indicating mean values and green dots indicating medians. Numbers correspond to the number of measurements for each rock group.

Connected porosity

Massive samples exhibit the lowest porosity (0.4–2.4%, mean 0.99%), while fractured samples form an intermediate cluster (1.2–6.4%, mean 2.65%; Figure 14). Similarly, altered-cemented and altered-replaced samples commonly remain below 3% porosity. Conversely, altered-porous samples show distinctly elevated porosities between 17–18%, forming a separate high-porosity field in Figure 15.

Permeability

Permeability measured at low confining pressure (~1 MPa) spans more than five orders of magnitude across the dataset and, globally, there is no obvious relationship between permeability and porosity (~8×10^{-18} to 6×10^{-13} m^2; Figure 14). Across all facies, permeability typically increases systematically with porosity (Figure 15), and the highest values are observed in fractured and altered-porous samples, where interconnected microfractures and dissolution vugs form the primary fluid pathways (Figures 5 and 9). Massive samples have the lowest average permeability values (~1.07×10^{-17} m^2) whereas altered-replaced and altered-cemented rocks also cluster around low values, in the order of 10^{-18} to 10^{-16} m^2. Fractured samples exhibit the widest range of permeability, as well as the highest values under low confining pressure (1.6×10^{-15} to 6.4×10^{-13} m^2), while altered porous samples show slightly lower values in the order of 10^{-17} to 10^{-15} m^2. Under increasing confining pressure, the permeability of the most permeable fractured samples decreases from high values on the order of 10^{-13} m^2 at 1 MPa towards 10^{-16} to 10^{-17} m^2 at 50 MPa (Figure 15). In contrast, the altered-porous facies exhibit much lower permeability reduction as a function of increasing confining pressure, decreasing from ~3.5×10^{-15} to ~2.0×10^{-15} m^2 between 1 and 50 MPa.



643

644 Figure 15 Petrophysical properties plotted against porosity for the five granitic facies of the Vehmaa rapakivi,
645 highlighting systematic variations linked to the proximity of faults and the distinct types of hydrothermal alteration.
646 Pc – confining pressure. Cp – specific heat capacity.

647 **Elastic Wave Velocities**

648 P-wave velocities (Vp) are generally highest in massive and altered-cemented rocks, with mean
649 values of ~5530 and ~5710 m s^{-1}, respectively (Figure 14). In detail, fractured and altered-replaced
650 samples show overlapping but slightly lower mean Vp values of ~5220 and ~5170 m s^{-1},
651 respectively, whereas altered-porous samples define the lowest range, from 4408 to 4721 m s^{-1},

652 with a mean of ~4550 m s^{-1}. S-wave velocities (Vs) broadly follow the same pattern where data
653 are available, with mean values of ~2960 m s^{-1} for massive rocks, ~2900 s^{-1} for altered-cemented
654 rocks, ~2860 s^{-1} for fractured rocks, and ~2670 s^{-1} for altered-replaced rocks.

655 **Magnetic Properties**

656 Magnetic susceptibility is highly heterogeneous, spanning nearly three orders of magnitude across
657 the dataset (Figure 14). Massive, fractured, and replaced samples largely overlap and display a
658 wide range of values. In contrast, altered porous samples consistently show low magnetic
659 susceptibility, whereas the altered cemented facies clusters at intermediate values. Magnetic
660 susceptibility shows only a weak relationship with porosity (Figure 15), although the lithofacies
661 define broadly distinctive clusters. Massive samples are characterized by low porosity but variable,
662 locally high magnetic susceptibility. Altered-porous samples form a high-porosity, low-
663 susceptibility cluster, whereas the low-to-moderate-porosity altered-cemented samples show
664 mostly magnetic susceptibility. Altered-replaced and fractured samples occupy low- to moderate-
665 porosity fields and show the widest scatter in magnetic susceptibility, including locally very high
666 values.

667 **Electrical Properties**

668 Electrical properties show a broad inverse relationship between electrical resistivity and
669 chargeability across the different facies (Figure 14). Massive granite has the highest electrical
670 resistivity and generally the lowest chargeability, whereas the altered-cemented facies shows the
671 lowest electrical resistivity and highest chargeability. Altered-porous samples also display
672 relatively low electrical resistivity and high chargeability. Altered-replaced and fractured samples

occupy intermediate and partly overlapping fields, with fractured samples showing a comparatively widespread in both properties.

Thermal Properties

Thermal conductivity varies systematically with lithofacies (Figure 14). Massive, fractured, and replaced granites generally show the highest and most variable thermal conductivity values. In contrast, altered-porous samples define the lowest values, usually below 2.0 W m^{-1} K^{-1}. Altered-cemented samples also show relatively low thermal conductivity despite their low porosity due to mineral precipitation. In the plot of thermal conductivity as a function of porosity, both dry and wet measurements show a negative relationship between thermal conductivity and porosity, from massive to altered samples (Figure 15).

Specific heat capacity (Cp) varies less strongly between lithofacies than thermal conductivity, but still shows systematic relationships with porosity and saturation state (Figure 14). Under dry conditions, Cp spans broadly from ~0.8 to 2.3 MJ m^{-3} K^{-1}, with massive and fractured granites generally clustering toward higher values. Altered samples extend toward lower dry Cp values, especially the altered-porous facies. Upon water saturation, Cp increases across most lithofacies, with many samples converging near ~2.0–2.4 MJ m^{-3} K^{-1} and the highest values occurring in the more porous samples.

6 Discussion

6.1 Multistage alteration and element mobilization

The Vehmaa Rapakivi Batholith records a multistage alteration evolution in which magmatic, structural, and hydrothermal processes strongly modified the original granitic fabric, producing

694 marked contrasts in reservoir properties such as porosity and permeability, as well as element
695 redistribution. Results from this study allow us to distinguish five main alteration stages: (1) late-
696 magmatic F-rich crystallization and deuteric alteration; (2) localized high-temperature alteration
697 and cementation; (3) fault-controlled propylitic alteration; (4) silica-rich brecciation and quartz
698 cementation; and (5) low-temperature oxidizing fracture and pore overprint. Rather than defining
699 a strict chronological sequence, these stages represent distinct alteration processes that may
700 overlap in time and space and recur during successive episodes of faulting and fluid circulation, as
701 detailed in the following sections.

702 **Stage 0: Progressive magmatic crystallization**

703 Stage 0 records the successive emplacement, crystallization, and differentiation of the Vehmaa
704 rapakivi melts between ca. 1.58 and 1.57 Ga, broadly at ~700–800 °C (Eklund and Shebanov,
705 1999), that is not directly related to secondary alteration and reservoir formation (Table 1). The
706 age of crystallization is confirmed by new U-Pb data from prismatic zircons, yielding an age of
707 1574 ± 8 Ma (Figure 13). Although the batholith was assembled through successive magmatic
708 pulses (Selonen et al., 2005), our results show that the massive, mainly-unaltered granite forms a
709 comparatively tight geochemical cluster across most major and minor elements (Figures 10 and
710 11) and therefore define the reference composition for assessing later alteration. The only two
711 massive granite samples showing MgO and K_2O outliers are aplitic dikes collected near the NW
712 contact of the batholith with the surrounding mica gneisses, and their anomalous compositions
713 may reflect local host-rock contamination or crystallization from a compositionally distinct melt.
714 The observed variability in TiO_2 and P_2O_5 is linked to the uneven distribution of Ti-bearing
715 accessory phases and apatite (Figures 4 and 10). SEM–EDS analyses further show that primary

716 REE are hosted mainly in monazite, apatite, and zircon, whereas Sn-bearing concentrations are
717 spatially associated with quartz-rich domains.

718 **Stage 1: Late-magmatic F-rich crystallization and deuteric alteration**

719 Stage 1 records the final crystallization of the Vehmaa Rapakivi Granite and limited deuteric
720 alteration through interaction with late-magmatic fluids (Table 1). As crystallization approached
721 completion, the residual melt became progressively enriched in F and other incompatible
722 components, as indicated by interstitial fluorite and minor topaz occupying intercrystalline spaces
723 (Figure 4). Textural evidence for localized deuteric alteration includes fine-grained fluorite
724 replacing plagioclase along cleavage planes, incipient sericitization of feldspars, and minor
725 chloritization of biotite (Figure 4). This stage probably dates at around 1570 Ma and during the
726 final crystallization of granite, although it has not been dated directly. An approximate temperature
727 range of 600–700 °C is inferred by comparison with the Kymi topaz granite, a late-stage F-rich
728 intrusion within the Wiborg Rapakivi Batholith, where melt-inclusion studies document the
729 evolution of a highly differentiated residual granitic melt (Lukkari et al., 2009).

730 **Stage 2: Localized high-temperature alteration and cementation**

731 Stage 2 is represented by the altered-cemented facies, where pyroxene, epidote, calcite, albite, and
732 sulphides form dense intergrowths that completely replace the primary granitic fabric (Figure 8),
733 These rocks are often associated with clinopyroxene–amphibole–titanite-chlorite veins and their
734 alteration halos (Figures 2, 5, and 6), and both consistently occur along strike-slip faults that
735 transect much of the batholith (Nordbäck et al., 2026). Comparable mineral assemblages and veins
736 are typical of high-temperature hydrothermal alteration and sub-solidus metasomatism, but their
737 formation temperatures vary widely among geological settings, from, for example, ~300 °C

propylitic alteration in the Salton Sea (California, USA) and Reykjanes (Iceland) geothermal systems (Caruso et al., 1988; Marks et al., 2010), to near-solidus conditions >650 °C in clinopyroxene-bearing episyenites of the Suomenniemi Rapakivi Complex (Suikkanen et al., 2019). U–Pb dating of secondary titanite collected from the altered-cemented granite yielded an age of 1595 ± 29 Ma, which overlaps the granite crystallization interval within analytical uncertainty (Figure 13, Table 1)

The relatively high-temperature alteration recorded by Stage 2 was accompanied by substantial but heterogeneous chemical modification of the granite. Compared with the massive granite, the altered-cemented facies shows much lower SiO_2 and substantially higher CaO, $Fe_2O_3^t$, Al_2O_3, S, Zn, Sn, Sr, La, and Ce, although these changes vary markedly among samples (Figures 10 and 11). The high CaO contents are consistent with abundant calcite cement and suggest interaction with CO_2-bearing fluids (Figure 8f). Some altered-cemented samples have SiO_2 contents up to ~20 wt.% lower than the massive granite, consistent with quartz dissolution and silica removal, as documented in episyenites of the Suomenniemi Rapakivi Complex (Suikkanen et al., 2019), although dilution by newly precipitated calcite and other secondary minerals may also contribute. Na_2O enrichment is coupled with K_2O depletion (Figure 10), reflecting albitization of K-feldspar (Figure 9b).

Stage 2 also produced pronounced but selective redistribution of trace elements (Figure 11). Strong S–Zn enrichment in the altered-cemented facies is linked to sulphide precipitation, particularly sphalerite (Figure 8d), whereas elevated Sn could not be linked to any discrete Sn-bearing mineral, such as cassiterite. Instead, Sn is consistently spatially associated with quartz-rich domains, suggesting a link between Sn redistribution and precipitation of hydrothermal quartz, although its mineral host remains unresolved. Bulk Pb concentrations remain relatively low despite the local

761 occurrence of galena (Figure 8d), indicating that Pb enrichment was limited. Higher La, Ce, and
762 Y concentrations point to mobilization and retention of REE, mainly within REE-rich epidote,
763 which is abundant in the altered-cemented facies (Figure 8) and may also contribute to the
764 observed Al_2O_3Al increase. Enrichment in REE, Zn, and Sn, together with local Pb mineralization,
765 is commonly reported in evolved A-type granites (Papoutsa and Piper, 2013; Yan et al., 2025),
766 including rapakivi granites in Finland (Haapala and Rämö, 2015).

767 **Stage 3: Fault-controlled propylitic alteration**

768 Stage 3 records intense propylitic alteration along fractures and faults and is expressed by the
769 altered-replaced and altered-porous facies, as well as by chlorite, titanite, epidote, amphibole, and
770 pyroxene bearing veins in fractured granites (Figures 2, 5, 6, 7, 9, and 12). The characteristic
771 assemblage of epidote, chlorite (mainly chamosite), sericite, albite, secondary quartz, fluorite, and
772 titanite is consistent with moderate-temperature hydrothermal alteration, for which a provisional
773 range of ~250–350 °C is inferred (e.g., Inoue et al., 2010; Nishimoto and Yoshida, 2010; Sanchez-
774 Alfaro et al., 2016). The onset of this stage was probably at least partially coeval with Stage 2, as
775 the U–Pb age of 1568 ± 9 Ma from a chlorite-titanite vein (Figures 5d and Figure 13) overlaps the
776 crystallization of the granitic body within analytical uncertainty (Table 1). Secondary zircon
777 analyses also fall within this age range, yielding a mean age of 1551 ± 12 Ma. A second titanite
778 age cluster is observed at 1000 ± 29 Ma (Figure 13), and together with its spatial association with
779 at least two generations of chlorite veins (Figure 5c), support a long-lived hydrothermal system,
780 occurring either continuously or through recurrent pulses for nearly 500 Myr. The ~1000 Ma age
781 cluster could alternatively record partial thermal resetting of the U–Pb system in the secondary
782 titanite rather than a distinct episode of titanite crystallization or alteration.

783 Overall, propylitic alteration produced substantial chemical changes, characterized by relative
784 increases in Al_2O_3, MgO, and Na_2O and decrease in SiO_2 and K_2O, while S and Zn enrichment is
785 generally weaker than in Stage 2 (Figures 10 and 11). These chemical transformations are
786 consistent with the mineralogical observations of chlorite replacing biotite, albitization of K-
787 feldspar, and sulphide precipitation within the altered-porous, replaced, and fractured rocks
788 (Figures 6f and 9). REE show additional redistribution during propylitic alteration, with HREE
789 (e.g., Tm, Eu, Yb) remaining in spatial association with zircon, whereas LREE (e.g., La, Nd, Ce)
790 are concentrated around apatite and within apatite-fluorite reaction borders (Figures 7e and f). The
791 association of LREE with fluorite bearing reaction zones and secondary REE bearing minerals
792 may therefore reflect local REE precipitation and retention during F rich alteration, as proposed
793 by Migdisov et al. (2016). Additionally, we observed that TiO_2, probably released during biotite
794 breakdown, was retained in titanite, rutile, and ilmenite (Figure 9e).

795 In detail, the Vuosnainen transect provides further evidence of geochemical changes linked to the
796 fault architecture, with the most pronounced element redistribution concentrated in the fault core,
797 whereas the surrounding damage zones record weaker and more heterogeneous changes (Figure
798 12). Although HDFZ granites often show multiple veins, they do not define a distinct geochemical
799 signature relative to the fractured granites (Figure 10), suggesting that increased fracture density
800 alone do not produce systematic whole-rock chemical modification.

801 **Stage 4: Silica-rich brecciation and quartz cementation**

802 Stage 4 records renewed brittle deformation accompanied by silica-rich hydrothermal activity,
803 provisionally placed at ~200–300 °C based on its spatial relationship with propylitic alteration,
804 although quartz precipitation can occur over a much broader temperature range in geothermal

805 systems (Stimac et al., 2015). Granular quartz veins crosscut the earlier propylitic assemblages
806 (Figure 6d) suggesting that its generation postdates Stage 3 at least locally, although overlapping
807 or cyclical precipitation of quartz with Stage 3 alteration remains possible. Quartz veins infilling
808 polyhedral microfractures further indicate hydraulic brecciation mechanisms (Figure 6d; Rowland
809 and Simmons, 2012).

810 The geochemical expression of Stage 4 is limited, as SiO_2 content in fractured samples with
811 pervasive quartz cementation are similar to those of the massive granite (Figure 9), suggesting that
812 silica redistribution was localized and volumetrically minor (Table 1). One exception is the
813 association of quartz-rich domains with elevated Sn concentrations, indicating that Sn
814 redistribution remained spatially linked to silica-rich domains still during Stage 4.

815 **Stage 5: Low-temperature oxidizing fracture and pore overprint**

816 Stage 5 records a late-oxidizing overprint event. This is evident from an assemblage of kaolinite,
817 goethite, Fe–Mn oxides, barite, Mn–Ce rich nodules, and other REE-bearing coatings along
818 fractures and pore walls (Figures 5f and 9f). Based on the temperature stability of comparable low-
819 temperature hydrothermal assemblages, this alteration likely formed below ~150 °C (Stimac et al.,
820 2015), consistent with the low-temperature, near surface formation of goethite documented by
821 Shuster et al. (2005), although no direct temperature or geochronological constraints are presently
822 available for Vehmaa. The origin of Stage 5 may reflect progressive cooling of the hydrothermal
823 system accompanied by increasing infiltration of meteoric water, either continuously or
824 episodically. This process may have persisted from the Proterozoic or been renewed during
825 Phanerozoic sedimentary burial and far-field hydrothermal circulation related to the Caledonian
826 Orogeny (Alm et al., 2005; Kukkonen et al., 2025). Continued low-temperature mineral–fluid

interaction along fractures is also consistent with Quaternary paleo-hydrogeological evidence from Olkiluoto (Sahlstedt et al., 2010), while later near-surface weathering and supergene alteration may have continued to the present day. Future work using (U–Th)/He dating of goethite (e.g., Shuster et al., 2005) could directly constrain the timing of Stage 5 and help distinguish between late hydrothermal, Phanerozoic, and younger supergene alteration.

Table 1: Summary of the five-stage alteration stages in the Vehmaa Rapakivi Batholith. The table outlines the interpreted temperature ranges and fluids, age constrains, diagnostic minerals, key microtextures, and element mobility that describe the progressive fluid–rock evolution controlling reservoir properties and mineralization in the Vehmaa Batholith. Stages are schematic and partially overlapping in time; boundaries represent shifts in dominant alteration regime rather than sharp temporal breaks.

Stage / event	Temperature and fluids	Temperature constraints and mineralogical proxies	Age constraints	Lithofacies	Key minerals	Textures / microstructures	Element redistribution relative to massive granite	Interpretation
0: Progressive magmatic crystallization	Crystallization and differentiation of an evolved granitic magma, broadly at ~700–800 °C.	Thermobarometry constrain of the rapakivi texture by Eklund and Shebanov (1999): inclusions in K-feldspar and quartz megacryst cores record ~680–720 °C at 5–8 kbar; whereas ovoid margins and plagioclase mantles record ~760–780 °C during decompression to ~3.5–1 kbar.	Zircon and monazite U–Pb dating yielded 1582 ± 4 Ma and 1573 ± 8 Ma (Selonen et al., 2005), constraining successive emplacement and crystallization of the Vehmaa rapakivi magmas between 1586 and 1565 Ma. New U-Pb data from prismatic zircons, yielding an age of 1574 ± 8 Ma	Massive granite varying from porphyritic, to course-grained granite and aplitic dikes.	K-feldspar, plagioclase, quartz and biotite; accessory zircon, monazite, apatite and Ti oxides.	Compact interlocking mosaic with sharp grain boundaries and negligible porosity. Zircon, monazite and apatite occur mainly as inclusions in biotite.	Massive samples form a comparatively tight cluster across most major and minor elements and define the reference composition. Mg and K outliers are from two aplitic-dike samples. Ti and P scatter reflects heterogeneous mineral distribution. Primary REE are hosted mainly by monazite, apatite, and zircon. Sn-bearing microphases are locally associated with quartz-rich domains.	Preservation of the primary magmatic mineralogical and geochemical signature. Zircon, monazite and apatite host primary REE and are potential sources for later remobilization.
1: Late-magmatic F-rich crystallization and deuteric alteration	Crystallization of an evolved, F-rich residual melt during the final stages of rapakivi granite crystallization, possibly at ~600–700 °C.	Interstitial fluorite and topaz indicate crystallization from an evolved F rich residual melt; the ~600–700 °C estimate is based on the Ilkyai topaz granite analogue, not direct thermometry for Vehmaa (Lukkari et al., 2009).	Probably close to ca. 1570 Ma, during final granite crystallization; no direct age has been assigned to this stage.	Massive, weakly altered granite.	Fluorite and minor topaz, locally associated with apatite, feldspar and biotite.	Fluorite and topaz occur mainly in interstitial domains and along plagioclase cleavage planes. Incipient sericitization of plagioclase and minor chloritization of biotite.	Localized and heterogeneous F concentrations, with little systematic element modification. REE redistribution by F-rich residual melt is possible but transfer has not been demonstrated.	Records final magmatic differentiation and localized alteration related with evolved F-rich residual melts.
2: Localized high-temperature alteration and cementation	Localized alteration pulses during the final cooling stages of the rapakivi granite at around 300–650 °C.	Broad temperature range based on mineral paragenesis and intergrowths of pyroxene, epidote, calcite, albite, and sulphides.	Titanite U–Pb dating of an altered-cemented sample yielded an age of 1585 ± 29 Ma, which overlaps the granite crystallization interval within analytical uncertainty. The alteration and cementation assemblage must postdate granite solidification because it occupies brittle fault structures.	Altered-cemented facies and pyroxene veins localized within NW-trending strike-slip faults.	REE-bearing epidote, pyroxene, amphibole, calcite, albite, K-feldspar, titanite, fluorite, apatite, sphalerite and galena.	Dense fine-grained intergrowths and cemented domains that completely obscure the primary granitic fabric.	Substantial Si reduction and relative increases in Ca, Fe, S, Zn, Sn, Sr, La, and Ce, with heterogeneous F and P redistribution. Carbonate precipitation records transfer of CO_2-bearing components, whereas localized sulphide precipitation records transport and deposition of metals.	Localized fault-hosted alteration and mineral precipitation produced dense cemented domains and locally reduced pore space and permeability.
3: Fault-controlled propylitic alteration	Moderate-temperature hydrothermal alteration at ~250–350 °C; fluid composition and pH are not directly constrained.	Working range inferred from precipitation of chlorite/chamosite, epidote, sericite, albite and multiple chlorite-titanite-epidote veins.	Partly coeval with Stage 2. Titanite and zircon U–Pb dating yielded two clusters at 1568 ± 9 Ma and 1000 ± 29 Ma, suggesting that propylitic alteration may have persisted for ~500 Myr after granite crystallization, either continuously or through recurrent hydrothermal pulses. Secondary zircon analyses also fall within this age range, yielding a mean age of 1551 ± 12 Ma.	Altered-recrystallized and altered-porous facies; fractured granite and high-density fracture zones containing chlorite-, titanite- and epidote-bearing veins.	Epidote, chlorite/chamosite, sericite, albite, secondary quartz, fluorite, titanite, rutile and ilmenite.	Pseudomorphic replacement of plagioclase by sericite and epidote; chloritization and dissolution of biotite; albitization of K-feldspar; sieve, intracrystalline, and vuggy porosity. Crosscutting relationships among multiple chlorite vein generations further support prolonged or recurrent fluid circulation.	Relative but heterogeneous increases in Mg and Na concentrations accompany decreasing Si and K, recording propylitization and albitization. Zn and S increases are generally weaker than in Stage 2. HREE remain preferentially associated with zircon, whereas LREE are concentrated around apatite, within apatite-fluorite reaction zones. Ti released during biotite alteration was retained in titanite, rutile and ilmenite.	Main propylitic replacement and dissolution. The balance between dissolution and precipitation generated secondary porosity in some domains and recrystallized or partly sealed others.
4: Silica-rich brecciation and quartz cementation	Silica-saturated hydrothermal fluids circulating during renewed brittle deformation, probably at ~200–300 °C	Quartz veins crossout the propylitic fabric, showing that at least the principal vein generation postdates Stage 3. The temperature range is inferred from its spatial relationship with propylitic alteration; no direct fluid-inclusion or quartz thermometry is presently available for Vehmaa.	The principal crosscutting quartz-vein generation at least partially postdates Stage 3. Local overlap with late Stage 3 activity is possible; not age constrained.	Typically with altered-recrystallized facies.	Quartz dominant.	Multidirectional quartz veins and locally brecciated, sealed or partly sealed fractures crosscutting primary and secondary mineral assemblages.	Relative silica enrichment reflects internal redistribution and/or external addition. quartz-rich domains locally contain Sn-bearing microphases.	Records renewed fracture opening, brecciation and subsequent partial to complete quartz sealing. It produced contrasting reservoir effects by maintaining connected fractures in some domains while occluding them in others.
5: Low-temperature oxidizing fracture and pore overprint	Low-temperature oxidizing fluids, probably below ~150 °C, circulating after the main hydrothermal stages and locally producing a supergene overprint.	Goethite, kaolinite, Fe oxyhydroxides and Mn oxides overprint earlier propylitic assemblages along fractures and pore walls support a low-temperature oxidizing environment, but <150 °C is an inferred upper limit. A supergene origin is compatible with the assemblage but is not uniquely demonstrated.	Postdates the main hydrothermal stages. No direct geochronological constraints are presently available.	Fractured granite, including locally open fracture networks, and altered-porous facies	Kaolinite, goethite, Mn-Fe oxides, barite and REE-bearing coatings or Mn-Ce-rich nodules.	Open or partly open microfractures and dissolution pores lined by kaolinite-goethite coatings. Fe-Mn-rich material and concentric Mn-Ce-rich nodules.	Localized LREE remobilization and scavenging on Mn oxides, Fe oxyhydroxides and clay-rich surfaces. Fe and Mn were redistributed into fracture- and pore-wall coatings	Late oxidizing overprint focused along fractures and pore networks that remained open or were reactivated. REE-bearing coatings record secondary remobilization and trapping; a locally supergene contribution is possible

6.2 Reservoir Formation, Evolution, and Prospectivity

This section links petrophysical properties to the alteration stages to provide a framework for evaluating how successive mineralogical and structural changes influence the formation and evolution of crystalline reservoirs. In particular, we assess parameters controlling the capacity of

842 the granite to store and transmit fluids and heat, together with key petrophysical properties relevant
843 to geophysical prospectivity, including elastic wave velocities and electrical and magnetic
844 properties, as well as fluid–rock reactions controlling element mobility and the potential
845 redistribution of critical elements in geothermal reservoirs.

846 **Reservoir Properties**

847 Density variations are primarily associated with mineral cementation and dissolution, whereas the
848 density of the fractured and replaced granites remains comparable to the massive granite (Figure
849 14), indicating that brittle deformation and pseudomorphic mineral replacement alone did not
850 substantially modify bulk density. This limited effect is consistent with fracture apertures that are
851 typically in the millimeter range and are commonly partially sealed by secondary minerals (Figures
852 3b, 5 and 6), in agreement with previous studies of reservoir rocks (McNamara et al., 2016;
853 Griffiths et al., 2016; Kushnir et al., 2023; Bischoff et al., 2024; Schuster et al., 2025). In contrast,
854 Stage 2 alteration substantially increased density through extensive mineral precipitation and
855 cementation, particularly by calcite, epidote, pyroxene, sphalerite, and Fe-oxides (Figure 8). Stage
856 3, at least locally, had the opposite effect, as dissolution and leaching generated secondary porosity
857 up to 18%, locally reducing bulk density (Figure 9). Stages 4 and 5 had only limited effects on
858 bulk density, as fractured rocks affected by quartz cementation and fracture coatings define a
859 relatively tight cluster comparable to the massive granite (Figure 14).

860 Unlike findings from the Suomenniemi granite, where episyenitization involved substantial quartz
861 dissolution during high-temperature (>650 °C) Na-metasomatism (Suikkanen et al., 2019),
862 preserved porosity in Vehmaa is primarily associated with Stage 3 propylitic alteration likely at
863 approximately 250–350 °C. This is because, in Vehmaa, fault-controlled propylitic alteration
864 induced reactions including chloritization of biotite and albitization of K-feldspar, which produced

865 rock-volume changes and mineral leaching that generated pervasive vuggy and sieve textures,
866 alongside extensive microfracturing (Figure 9), as previously reported for crystalline rocks
867 affected by hydrothermal alteration (Inoue et al., 2010; Morad et al., 2011; Bischoff et al., 2024).
868 Pseudomorphic replacement of feldspar by sericite and epidote also generated sieve porosity in the
869 altered-replaced rocks (Figure 7c), although its effect on bulk porosity remained limited to <3%
870 volume (Figure 14). Quartz dissolution is inferred by the lower SiO_2 content of the altered-porous
871 facies relative to the massive granite (Figure 10), particularly because much of the quartz present
872 in the altered-porous facies occurs as secondary precipitates on pore walls (Figure 9b). Additional
873 local porosity reduction also occurred where remobilized Ti, Fe, and Na precipitated as secondary
874 oxides and albite (Figure 9). Although the low Si content of the altered-cemented facies suggests
875 that quartz removal and secondary porosity generation may also have occurred during Stage 2
876 (Figure 14). Pervasive precipitation of calcite, sulphides, albite, and quartz occluded most of the
877 available pore space still during Stage 2, locally producing a tightly cemented rock with little to
878 no preserved porosity (Figure 8). Subsequent Stages 4 and 5 further reduced porosity through
879 precipitation of quartz, Fe oxides, REE bearing phases, and late alteration clays (Figures 5, 6, and
880 9f), or generate additional secondary porosity by replacement of silicate by Fe-oxyhydroxides,
881 contributing to the broad spread of porosity values observed in fractured rocks (Figure 14).

882 The permeability data emphasize that the capacity of the Vehmaa granite to transmit fluids reflects
883 the combined effects of brittle deformation and alteration styles rather than fracture abundance
884 alone (Bourbie and Zinszner, 1985: Nelson, 1994; Heap et al., 2017). While fracturing creates
885 highly connected flow pathways at low confining pressure (Figure 14), fractured samples show a
886 marked permeability reduction already by ~10 MPa, followed by a continued decrease with
887 increasing pressure (Figure 15), reflecting the progressive mechanical closure of fractures with

888 increasing burial depths (Nara et al., 2011; Achtziger-Zupančič et al., 2017; Carbillet et al., 2025a).
889 In contrast, the altered-porous facies is much less sensitive to confining pressure, indicating that
890 its high-permeability is maintained by a more mechanically stable pore network generated during
891 Stage 3 alteration (Figure 9), and consistent with observations from altered crystalline reservoirs
892 elsewhere (Bischoff et al., 2024; Carbajal Martinez et al., 2026). Indeed, due to their geometry and
893 aspect ratio, microcracks and macrocracks are much easier to close than pores as confining
894 pressure (i.e., depth) is increased. Previous studies have documented how the permeability of a
895 granite can increase resulting from alteration-induced mineral dissolution (Sausse et al., 2001;
896 Nishimoto and Yoshida, 2010; Farquharson et al., 2020; Sanchez-Roa et al., 2021). Conversely,
897 mineral precipitation and recrystallization during Stages 2 and 3, followed by local quartz
898 cementation during Stage 4, progressively reduced or sealed preexisting flow pathways (Figures
899 6d and 8). Void-filling mineral precipitation has previously been shown to reduce the permeability
900 of rock, including granite (Morrow et al., 2001; Noiriel et al., 2016; Griffiths et al., 2016; Heap et
901 al., 2019; Kushnir et al., 2023). Stage 5 had a dual effect on permeability: replacement of primary
902 silicate minerals by Fe-oxyhydroxides can locally enlarge the pore network, particularly in the
903 HDFZ rocks (Figure 6a), whereas precipitation of REE-rich phases, Mn-Fe oxides, goethite, and
904 kaolinite reduced the pore throat-ratio and connectivity (Figures 5 and 9f). Indeed, there is no
905 simple relationship between permeability and porosity (Figure 15); typically, the permeability of
906 rock increases as a function of increasing porosity (e.g., Bourbie and Zinszner, 1985; Nelson, 1994;
907 Heap et al., 2017). Although not tested here, we also highlight that temperatures higher than
908 ambient can close microcracks in granite, due to mineral thermal expansion, and reduce
909 permeability (Carbillet et al., 2025b).

910

Geophysical Signature

The lower elastic wave velocities of the altered-porous and fractured facies are primarily attributed to secondary porosity developed during Stage 3, which reduce both Vp and Vs (Figures 14 and 15) and consistent with previous studies (Moos and Zoback, 1983; Farquharson et al., 2020). Mineral replacement during this stage may further modify the elastic response, particularly where feldspars are replaced by sericite and epidote (Figure 7). In contrast, mineral precipitation during Stage 2, and locally during Stages 4 and 5, may partly counteract these effects by filling pores and sealing fractures. In the altered-cemented facies, this process produced a dense rock mass with elastic wave velocities comparable or higher to those of the original massive granite (Figure 14).

Stage 2 produced the clearest mineralogical control on the electrical response, where extensive cementation by calcite, epidote, pyroxene, albite, sulphides, and Fe-bearing phases generated rocks with relatively low electrical resistivity and high chargeability despite their low porosity. Conversely, interconnected pores generated during Stage 3 facilitate electrical conduction through the wet pore network, while sericite, chlorite, and other fine grained alteration minerals may also contribute to polarization. The consistently low magnetic susceptibility associated with the more porous rocks suggests that dissolution and replacement also redistribute Fe-bearing minerals into secondary phases with a weaker bulk magnetic response. In contrast, the broad overlap in magnetic susceptibility among massive, fractured, and replaced rocks indicates that fracturing and pseudomorphic mineral replacement alone did not systematically modify the magnetic properties of the granite. Quartz precipitation during Stage 4 does not show direct influence on magnetic susceptibility and electric properties while the precipitation of goethite, Mn-Fe oxides, and kaolinite during Stage 5 introduced additional electrically active mineral surfaces and may contribute to the heterogeneous chargeability response seeing in the fractured rocks. Similarly, the

influence of Stage 5 on magnetic susceptibility is likely more variable and dependent on the abundance and specific mineralogy of the Fe-bearing phases precipitated within the fractures.

Because these alteration processes modify both pore structure and minerals, these processes also generate physical contrasts that may be detectable using geophysical methods. For example, Stage 3 alteration, characterized by secondary porosity and fracturing, produce substantial Vp and Vs reduction, likely generating strong impedance contrasts with the surrounding massive granite that could be targeted by seismic surveys (Schreiter et al. (2015). In contrast, zones affected by extensive Stage 2 cementation may show elastic wave velocities similar to the massive granite and therefore produce a much weaker impedance contrast. Magnetotelluric (MT) surveys may complement seismic imaging by identifying conductive alteration zones (Samrock et al. 2015), although low resistivity alone cannot confidently distinguish between porous, fluid filled rocks and strongly cemented mineralized domains.

Thermal Properties

As observed for the other petrophysical properties, thermal conductivity and heat capacity are strongly influenced by the competing alteration effects and are comparatively less affected by fracturing, as commonly reported for most rocks (e.g., Heap et al., 2022, 2023; Bischoff et al., 2024). Fractured and replaced rocks remain comparable to the massive facies, indicating that fracturing and pseudomorphic mineral replacement alone have only a limited effect on thermal properties. Stage 3 produced the clearest reduction in thermal conductivity, as secondary porosity disrupted the original high-conductive quartz–feldspar framework, while replacement by chlorite, sericite, and other alteration minerals may further reduced heat transport (Figure 9). Thermal conductivity also remains relatively low in the altered-cemented facies, even though Stage 2 involved extensive mineral precipitation and cementation by calcite, epidote, fluorite, sulphides,

and pyroxene, indicating that these processes did not re-establish a continuous conductive framework (Figure 8). Heat capacity is less sensitive to alteration and is more strongly influenced by pore volume and fluid saturation (Figure 15). Secondary porosity reduces the mineral volume available for heat storage under dry conditions, whereas saturation compensates for this effect because water occupying pores contributes substantially to bulk heat capacity, as previously observed by Heap et al., (2020). Consequently, secondary porosity can reduce conductive heat transport while simultaneously increasing the importance of pore fluids for thermal storage.

6.3 Co-Production of Geothermal Energy and Critical Elements

The combined petrophysical, mineralogical, and geochemical data indicate that fault-controlled alteration represents a key target for both geothermal and critical element exploration. Porous and fractured rocks provide the principal pathways for fluid and heat transport (Sibson, 1996), while the same hydrothermal systems can promote mobilization and local enrichment of economically relevant elements, including Li, Rb, and REE (Migdisov et al., 2016; Sanjuan et al., 2022; Sajkowski et al., 2023).

In this context, the spatial association between reservoir formation, fluid–rock interaction, and element redistribution suggests that the co-production of geothermal energy and critical elements may, in principle, be feasible within the same fault-controlled hydrothermal system. However, this potential depends on whether economically relevant elements can be mobilized from the rock and remain sufficiently soluble in geothermal fluids under reservoir and production conditions (Szanyi et al., 2023). Co-production of lithium from geothermal brines is already advancing toward commercial scale, with ongoing projects in crystalline reservoirs of the Upper Rhine Graben (France–Germany–Switzerland) and Cornwall (UK) demonstrating the transition from pilot

testing toward integrated geothermal energy and lithium production (Kölbel et al., 2023; Sanjuan et al., 2026).

Beyond lithium, co-production of other economically relevant elements from geothermal brines remains at an earlier stage of development. Elements such as Rb, Cs, Sr, Zn, Mn, Sb, and REE have been identified as potential co-products, but their recovery is generally less mature particularly because of the lower dissolved concentrations and more demanding separation requirements (Smith et al., 2017; Sajkowski et al., 2023). Ultimately, the viability of co-production will depend on the entire value chain, from element mobilization within the reservoir and transport through the wellbore without premature precipitation or scaling, to selective recovery and concentration at the surface into feedstocks suitable for downstream processing.

7 Conclusions

The Vehmaa Rapakivi Batholith shows that the formation and evolution of crystalline reservoirs depend on the combined effects of brittle deformation and long-lived fluid–rock interaction. Distinguishable alteration stages had a dual effect, either creating or destroying reservoir properties. High-temperature alteration during Stage 2 promoted extensive mineral precipitation and cementation, characterized by pyroxene, REE-rich epidote, calcite, albite, fluorite, and sulphides, particularly sphalerite. In contrast, Stage 3 propylitic alteration generated the most significant secondary porosity through mineral dissolution, replacement of biotite to chlorite and feldspar to sericite, and microfracturing. U–Pb ages from secondary titanite and zircon place Stage 2 and the onset of Stage 3 broadly overlapping with the crystallization of the Vehmaa granite at ~1.57 Ga, indicating that fault-controlled hydrothermal alteration began during the final stages of crystallization and early cooling of the batholith. These ages also provide chronological constraints

on the strike-slip fault systems identified by Nordbäck et al. (2024, 2026), placing their development within the waning phase of rapakivi magmatism. A younger titanite age cluster at ~1.0 Ga suggests that fluid–rock interaction was persistent or renewed much later in the history of the batholith, although partial thermal resetting of the titanite U–Pb system during the Sveconorwegian orogeny cannot be excluded. Later quartz cementation and low-temperature oxidizing alteration further modified petrophysical and geochemical signatures through localized precipitation of REE-bearing phases, goethite, and kaolinite. The major strike-slip faults transect much of the Vehmaa Rapakivi Batholith and control kilometer-scale fracture and alteration zones, suggesting that such reservoir development may extend over rock volumes relevant to industrial geothermal exploitation. Fluid circulation through these faults was also accompanied by substantial element redistribution. The strongest enrichments include REE, particularly La and Ce, together with Sc, Sr, Sn, and Zn, while Cd and Pb are more locally concentrated. Mineralization concentrated along fractures, pore walls, and vein margins may be underestimated by whole-rock geochemistry alone, highlighting the value of integrating bulk analyses with mineralogical mapping when evaluating prospective zones. Collectively, the Vehmaa Rapakivi Batholith demonstrates how prolonged and recurrent fluid flow along major faults can sustain pathways for heat and fluids over hundreds of millions of years while simultaneously promoting the redistribution and concentration of economically relevant elements. This dual effect provides a strong basis for targeting crystalline basement reservoirs for the co-production of geothermal energy and critical elements, thereby supporting the development of secure, low-carbon energy and mineral resources required for the energy transition.

8 Acknowledgements

This research was funded by the Research Council of Finland under the project "Deep-HEAT-Flows: Discovering Deep Geothermal Resources in Low-Enthalpy Crystalline Settings" (Decision No. 354356). The geochronological analyses were supported by the project "FLOP2 – Understanding Reactive Flow in Fractured Crystalline Bedrock for Safe Nuclear Waste Repositories", funded by the Finnish Nuclear Waste Management Fund as part of the SAFER2028 nuclear safety research programme (Decision No. SAFER 17/2026). Students Marion Spitz, Marianne Leon-Stackow, Hugo Zorninger, Aurélien Faury, Lara Juin, Matéo Dos, Hippolyte Carré, and Marie-Hanaé Villette from the University of Strasbourg, France, are gratefully acknowledged for their assistance in the field and with sample preparation for geochemical and petrophysical analyses. Students Maria Mäkelä, Laura Suvanto, and Mia Leminen from the University of Turku are thanked for their contributions to the Geoenergy Research Group. M. Heap acknowledges support from the Institut Universitaire de France (IUF) and from the Interdisciplinary Thematic Institute GeoT, as part of the ITI 2021–2028 programme of the University of Strasbourg, CNRS, and Inserm. The GeoT ITI was supported by IdEx Unistra (ANR-10-IDEX-0002) and by the SFRI-STRAT'US project (ANR-20-SFRI-012) under the framework of the French Investments for the Future Programme. XCT and μXRF were funded by the Research Council of Finland via the RAMI infrastructure grants #293109 and #337560, respectively.

9 Data availability

The XCT data are available via the Fairdata-PAS service at https://doi.org/10.23729/fd-7aa23433-fe11-3e91-b0bb-29f19763dfb3, and the μXRF data are available at https://doi.org/10.23729/fd-7fb4248c-4bec-3b4f-aa82-bcfd8726ab01. SEM-EDS, digital thin sections, and photos are in process to be included in a repository, which will be completed during the review process.

10 References

Aaltonen, I., Front, K., Gehör, S., & Sahlstedt, E. (2018). Hydrothermal alteration of bedrock at Olkiluoto. Posiva Report 2018-03. Posiva Oy, Eurajoki, Finland.

Abersteiner, A., Rämö, O.T., Kontonikas-Charos, A., Kharkongor, M., Karampelas, N., Gilbert, S.E., Wade, B., Ambroziak-Murzyn, K., Lloyd, J.C., Beier, C., & Glorie, S. (2025). Geochronological and geochemical insights into episyenite metasomatic overprint in the Proterozoic Suomenniemi rapakivi granite complex (Finland). Lithos, 516–517, 108269. https://doi.org/10.1016/j.lithos.2025.108269

Åhäll, K.-I., Connelly, J.N., & Brewer, T.S. (2000). Episodic rapakivi magmatism due to distal orogenesis? Correlation of 1.69–1.50 Ga orogenic and inboard "anorogenic" events in the Baltic Shield. Geology, 28, 823–826. https://doi.org/10.1130/0091-7613(2000)28<823:ERMDTD>2.0.CO;2

Alm, E., Huhma, H., & Sundblad, K. (2005). Preliminary Palaeozoic Sm–Nd ages of fluorite–calcite–galena veins in the southeastern part of the Fennoscandian Shield. SKB Report R-04-27. Svensk Kärnbränslehantering AB, Stockholm, Sweden.

Berni, G.V., Wagner, T., Fusswinkel, T., & Wenzel, T. (2017). Magmatic-hydrothermal evolution of the Kymi topaz granite stock, SE Finland: Mineral chemistry evidence for episodic fluid exsolution. Lithos, 292–293, 401–423. https://doi.org/10.1016/j.lithos.2017.09.015

Berni, G.V., Wagner, T., & Fusswinkel, T. (2020). From a F-rich granite to a NYF pegmatite: Magmatic-hydrothermal fluid evolution of the Kymi topaz granite stock, SE Finland. Lithos, 364–365, 105538. https://doi.org/10.1016/j.lithos.2020.105538

Bischoff, A., Heap, M.J., Mikkola, P., Kuva, J., Reuschlé, T., Jolis, E.M., Engström, J., Reijonen, H., & Leskelä, T. (2024). Hydrothermally altered shear zones: A new reservoir play for the expansion of deep geothermal exploration in crystalline settings. Geothermics, 118, 102895. https://doi.org/10.1016/j.geothermics.2023.102895

Carbajal-Martínez, D., Heap, M.J., Jolis, E.M., Luoto, T., Reuschlé, T., Vuoriainen, S., et al. (2026). Porous and permeable crystalline basement: Evidence for large-scale hydraulic connectivity at Kivetty, Finland. Journal of Geophysical Research: Solid Earth, 131, e2026JB034512. https://doi.org/10.1029/2026JB034512

Caruso, L.J., Bird, D.K., Cho, M., & Liou, J.G. (1988). Epidote-bearing veins in the State 2–14 drill hole: Implications for hydrothermal fluid composition. Journal of Geophysical Research: Solid Earth, 93, 13123–13133. https://doi.org/10.1029/JB093iB11p13123

Caspari, E., Greenwood, A., Baron, L., Egli, D., Toschini, E., Hu, K., & Holliger, K. (2020). Characteristics of a fracture network surrounding a hydrothermally altered shear zone from geophysical borehole logs. Solid Earth, 11, 829–854. https://doi.org/10.5194/se-11-829-2020

Cox, S.F. (2005). Coupling between deformation, fluid pressures, and fluid flow in ore-producing hydrothermal systems at depth in the crust. In Economic Geology 100th Anniversary Volume, 39–75. https://doi.org/10.5382/AV100.04

Corfu, F., Hanchar, J. M., Hoskin, P. W., & Kinny, P. (2003). Atlas of zircon textures. Reviews in mineralogy and geochemistry, 53(1), 469-500. https://doi.org/10.2113/0530469

Eklund, O., & Shebanov, A.D. (1999). The origin of rapakivi texture by sub-isothermal decompression. Precambrian Research, 95, 129–146. https://doi.org/10.1016/S0301-9268(98)00130-2

Green, P.F., Japsen, P., Bonow, J.M., Chalmers, J.A., Duddy, I.R., & Kukkonen, I.T. (2022). The post-Caledonian thermo-tectonic evolution of Fennoscandia. Gondwana Research, 107, 201–234. https://doi.org/10.1016/j.gr.2022.03.007

Haapala, I., & Lukkari, S. (2005). Petrological and geochemical evolution of the Kymi stock, a topaz granite cupola within the Wiborg rapakivi batholith, Finland. Lithos, 80, 347–362. https://doi.org/10.1016/j.lithos.2004.05.012

Haapala, I., & Rämö, O.T. (2015). Mineral deposits related to granitic rocks. In W.D. Maier, R. Lahtinen, & H. O'Brien (Eds.), Mineral Deposits of Finland (pp. 531–556). Elsevier, Amsterdam. https://doi.org/10.1016/B978-0-12-410438-9.00021-2

Harpers, N., Forbes Inskip, N., Allen, M.J., Buckman, J., Faulkner, D.R., Claes, H., Shail, R., den Hartog, S., & Busch, A. (2024). Effects of chemical alteration on frictional properties in a deep, granitic, geothermal system in Cornwall: Direct shear experiments at near in situ conditions. Journal of Geophysical Research: Solid Earth, 129. https://doi.org/10.1029/2024JB028861

Heap, M.J., Kushnir, A.R.L., Vasseur, J., Wadsworth, F.B., Harlé, P., Baud, P., Kennedy, B.M., Troll, V.R., & Deegan, F.M. (2020). The thermal properties of porous andesite. Journal of Volcanology and Geothermal Research, 398, 106901. https://doi.org/10.1016/j.jvolgeores.2020.106901

Heap, M.J., Jessop, D.E., Wadsworth, F.B., Rosas-Carbajal, M., Komorowski, J.C., Gilg, H.A., et al. (2022). The thermal properties of hydrothermally altered andesites from La Soufrière de Guadeloupe (Eastern Caribbean). Journal of Volcanology and Geothermal Research, 421, 107444. https://doi.org/10.1016/j.jvolgeores.2021.107444

Heap, M.J., Wadsworth, F.B., & Jessop, D.E. (2023). The thermal conductivity of unlithified granular volcanic materials: The influence of hydrothermal alteration and degree of water saturation. Journal of Volcanology and Geothermal Research, 435, 107775. https://doi.org/10.1016/j.jvolgeores.2023.107775

Inoue, A., Kurokawa, K., & Hatta, T. (2010). Application of chlorite geothermometry to hydrothermal alteration in Toyoha geothermal system, southwestern Hokkaido, Japan. Resource Geology, 60, 52–70. https://doi.org/10.1111/j.1751-3928.2010.00114.x

Jolie, E., Scott, S., Faulds, J., Chambefort, I., Axelsson, G., Gutiérrez-Negrín, L.C., Regenspurg, S., Ziegler, M., Ayling, B., Richter, A., & Zemedkun, M.T. (2021). Geological controls on geothermal resources for power generation. Nature Reviews Earth & Environment, 2, 324–339. https://doi.org/10.1038/s43017-021-00154-y

Kölbel, L., Kölbel, T., Herrmann, L., Kaymakci, E., Ghergut, I., Poirel, A., & Schneider, J. (2023). Lithium extraction from geothermal brines in the Upper Rhine Graben: A case study of potential and current state of the art. Hydrometallurgy, 221, 106131. https://doi.org/10.1016/j.hydromet.2023.106131

Korja, A., Korja, T., Luosto, U., & Heikkinen, P. (1993). Seismic and geoelectric evidence for collisional and extensional events in the Fennoscandian Shield: Implications for Precambrian crustal evolution. Tectonophysics, 219, 129–152. https://doi.org/10.1016/0040-1951(93)90292-R

Kraal, K.O., Ayling, B.F., Blake, K., Hackett, L., Perdana, T.S.P., & Stacey, R. (2021). Linkages between hydrothermal alteration, natural fractures, and permeability: Integration of borehole data for reservoir characterization at the Fallon FORGE EGS site, Nevada, USA. Geothermics, 89, 101946. https://doi.org/10.1016/j.geothermics.2020.101946

Kukkonen, I.T., et al. (2025). Phanerozoic evolution of Fennoscandia: Evidence from apatite fission track, fluid flow and geodynamic data in Finland and Estonia. Gondwana Research. https://doi.org/10.1016/j.gr.2025.05.011

Kushnir, A.R.L., Heap, M.J., Baud, P., Reuschlé, T., & Schmittbuhl, J. (2023). Reactivation of variably sealed joints and permeability enhancement in geothermal reservoir rocks. Geothermal Energy, 11, 32. https://doi.org/10.1186/s40517-023-00271-5

Kuva, J., Siitari-Kauppi, M.K., Lindberg, A., Aaltonen, I., Turpeinen, T., Myllys, M., & Timonen, J. (2012). Microstructure, porosity and mineralogy around fractures in Olkiluoto bedrock. Engineering Geology, 139–140, 28–37. https://doi.org/10.1016/j.enggeo.2012.04.008

Lahtinen, R., Korja, A., Nironen, M., & Heikkinen, P. (2009). Palaeoproterozoic accretionary processes in Fennoscandia. Geological Society, London, Special Publications, 318, 237–256. https://doi.org/10.1144/SP318.8

Lukkari, S., Thomas, R., & Haapala, I. (2009). Crystallization of the Kymi topaz granite stock within the Wiborg rapakivi granite batholith, Finland: Evidence from melt inclusions. Canadian Mineralogist, 47, 1359–1374. https://doi.org/10.3749/canmin.47.6.1359

Manning, C.E., & Ingebritsen, S.E. (1999). Permeability of the continental crust: Implications of geothermal data and metamorphic systems. Reviews of Geophysics, 37, 127–150. https://doi.org/10.1029/1998RG900002

Marks, N., Schiffman, P., Zierenberg, R.A., Franzson, H., & Friðleifsson, G.Ó. (2010). Hydrothermal alteration in the Reykjanes geothermal system: Insights from Iceland Deep Drilling Program well RN-17. Journal of Volcanology and Geothermal Research, 189, 172–190. https://doi.org/10.1016/j.jvolgeores.2009.10.018

Mattila, J., & Viola, G. (2014). New constraints on 1.7 Gyr of brittle tectonic evolution in southwestern Finland derived from a structural study at the site of a potential nuclear waste repository (Olkiluoto Island). Journal of Structural Geology, 67, 50–74. https://doi.org/10.1016/j.jsg.2014.07.003

Migdisov, A., Williams-Jones, A.E., Brugger, J., & Caporuscio, F.A. (2016). Hydrothermal transport, deposition, and fractionation of the REE: Experimental data and thermodynamic calculations. Chemical Geology, 439, 13–42. https://doi.org/10.1016/j.chemgeo.2016.06.005

Moos, D., & Zoback, M.D. (1983). In situ studies of velocity in fractured crystalline rocks. Journal of Geophysical Research: Solid Earth, 88, 2345–2358. https://doi.org/10.1029/JB088iB03p02345

Morad, S., Sirat, M., El-Ghali, M.A.K., & Mansurbeg, H. (2011). Chloritization in Proterozoic granite from the Äspö Laboratory, southeastern Sweden: Record of hydrothermal alterations and implications for nuclear waste storage. Clay Minerals, 46, 495–513. https://doi.org/10.1180/claymin.2011.046.3.495

Nara, Y., Meredith, P.G., Yoneda, T., & Kaneko, K. (2011). Influence of macro-fractures and micro-fractures on permeability and elastic wave velocities in basalt at elevated pressure. Tectonophysics, 503, 52–59. https://doi.org/10.1016/j.tecto.2010.09.027

Nironen, M. (1997). The Svecofennian Orogen: A tectonic model. Precambrian Research, 86, 21–44. https://doi.org/10.1016/S0301-9268(97)00039-9

Nishimoto, S., & Yoshida, H. (2010). Hydrothermal alteration of deep fractured granite: Effects of dissolution and precipitation. Lithos, 115, 153–162. https://doi.org/10.1016/j.lithos.2009.11.015

Nordbäck, N., Mattila, J., Zwingmann, H., & Viola, G. (2022). Precambrian fault reactivation revealed by structural and K–Ar geochronological data from the spent nuclear fuel repository in Olkiluoto, southwestern Finland. Tectonophysics, 824, 229208. https://doi.org/10.1016/j.tecto.2022.229208

Nordbäck, N., Skyttä, P., Engström, J., Ovaskainen, N., Mattila, J., & Aaltonen, I. (2024). Mesoproterozoic strike-slip faulting within the Åland rapakivi batholith, southwestern Finland. Tektonika, 2, 1–26. https://doi.org/10.55575/tektonika2024.2.1.51

Nordbäck, N., Bischoff, A., Carbajal-Martínez, D., et al. (2026). Strike-slip faulting and hydrothermal alteration in a Proterozoic rapakivi batholith: Implications for reservoir formation and geothermal exploration in crystalline cratons—Part 1. Geothermal Energy, 14, 1. https://doi.org/10.1186/s40517-025-00370-5

Papoutsa, A.D., & Pe-Piper, G. (2013). The relationship between REE–Y–Nb–Th minerals and the evolution of an A-type granite, Wentworth Pluton, Nova Scotia. American Mineralogist, 98, 444–462. https://doi.org/10.2138/am.2013.3972

Pokki, J., Kohonen, J., Lahtinen, R., Rämö, O.T., & Andersen, T. (2013). Petrology and provenance of the Mesoproterozoic Satakunta Formation, SW Finland. Geological Survey of Finland, Espoo.

Rämö, O.T. (1991). Petrogenesis of the Proterozoic rapakivi granites and related basic rocks of southeastern Fennoscandia: Nd and Pb isotopic and general geochemical constraints. Bulletin of the Geological Survey of Finland, 355.

Rämö, O.T., & Haapala, I. (1995). One hundred years of rapakivi granite. Mineralogy and Petrology, 52, 129–185. https://doi.org/10.1007/BF01163243

Rowland, J.V., & Simmons, S.F. (2012). Hydrologic, magmatic, and tectonic controls on hydrothermal flow, Taupo Volcanic Zone, New Zealand: Implications for the formation of epithermal vein deposits. Economic Geology, 107, 427–457. https://doi.org/10.2113/econgeo.107.3.427

Sahlstedt, E., Karhu, J.A., & Pitkänen, P. (2010). Indications for the past redox environments in deep groundwaters from the isotopic composition of carbon and oxygen in fracture calcite, Olkiluoto, SW Finland. Isotopes in Environmental and Health Studies, 46, 370–391. https://doi.org/10.1080/10256016.2010.505981

Sajkowski, L., Turnbull, R., & Rogers, K. (2023). A review of critical element concentrations in high-enthalpy geothermal fluids in New Zealand. Resources, 12, 68. https://doi.org/10.3390/resources12060068

Samrock, F., Kuvshinov, A., Bakker, J., Jackson, A., & Fisseha, S. (2015). 3-D analysis and interpretation of magnetotelluric data from the Aluto-Langano geothermal field, Ethiopia. Geophysical Journal International, 202(3), 1923–1948. https://doi.org/10.1093/gji/ggv270

Sanchez-Alfaro, P., Reich, M., Arancibia, G., Pérez-Flores, P., Cembrano, J., Driesner, T., Lizama, M., Rowland, J., Morata, D., Heinrich, C.A., Tardani, D., & Campos, E. (2016). Physical, chemical and mineralogical evolution of the Tolhuaca geothermal system, southern Andes, Chile: Insights into the interplay between hydrothermal alteration and brittle deformation. Journal of Volcanology and Geothermal Research, 324, 88–104. https://doi.org/10.1016/j.jvolgeores.2016.05.009

Sanjuan, B., Gourcerol, B., Millot, R., Rettenmaier, D., Jeandel, E., & Rombaut, A. (2022). Lithium-rich geothermal brines in Europe: An update about geochemical characteristics and implications for potential Li resources. Geothermics, 101, 102385. https://doi.org/10.1016/j.geothermics.2022.102385

Sanjuan, B., Millot, R., Genter, A., Dezayes, C., & Lerouge, C. (2026). Updated evaluation of the potential resources of geothermal lithium (Li) and rubidium (Rb) in the Upper Rhine Graben (URG). Geothermics, 140, 103724. https://doi.org/10.1016/j.geothermics.2026.103724

Schreiter, L., Hloušek, F., Hellwig, O., & Buske, S. (2015). Characterization of seismic reflections from faults in a crystalline environment, Schneeberg, Germany. Geophysical Prospecting, 63(4), 1015–1032. https://doi.org/10.1111/1365-2478.12255

Schuster, V., Rybacki, E., Schleicher, A.M., Koirala, R., & Göbel, T.H.W. (2025). The effect of hydrothermal alteration and microcracks on hydraulic properties and poroelastic deformation: A case study of the Blue Mountain Geothermal Field. Journal of Geophysical Research: Solid Earth, 130, e2024JB030541. https://doi.org/10.1029/2024JB030541

Selonen, O., Ehlers, C., Luodes, H., & Lerssi, J. (2005). The Vehmaa rapakivi granite batholith—An assemblage of successive intrusions indicating a piston-type collapsing centre. Bulletin of the Geological Society of Finland, 77, 65–70. https://doi.org/10.17741/bgsf/77.1.004

Shuster, D.L., Vasconcelos, P.M., Heim, J.A., & Farley, K.A. (2005). Weathering geochronology by (U–Th)/He dating of goethite. Geochimica et Cosmochimica Acta, 69, 659–673. 10.1016/j.gca.2004.07.028

Sibson, R.H. (1996). Structural permeability of fluid-driven fault-fracture meshes. Journal of Structural Geology, 18, 1031–1042. https://doi.org/10.1016/0191-8141(96)00032-6

Smith, Y.R., Kumar, P., & McLennan, J.D. (2017). On the extraction of rare earth elements from geothermal brines. Resources, 6, 39. https://doi.org/10.3390/resources6030039

Stimac, J., Goff, F., & Goff, C.J. (2015). Intrusion-related geothermal systems. In H. Sigurdsson, B. Houghton, S. McNutt, H. Rymer, & J. Stix (Eds.), The Encyclopedia of Volcanoes (2nd ed.). Academic Press. 10.1016/B978-0-12-385938-9.00046-8

Suikkanen, E., Rämö, O.T., Ahtola, T., & Lintinen, P. (2019). Clinopyroxene episyenites in a Proterozoic rapakivi granite, SE Finland—Recrystallization textures, mass transfer and implications for the petrology of A-type granite complexes. Mineralogy and Petrology, 113, 727–743. https://doi.org/10.1007/s00710-019-00684-w

1233 Suominen, V. (1991). The chronostratigraphy of southwestern Finland: With special reference to
1234 Postjotnian and Subjotnian diabases. Bulletin of the Geological Survey of Finland. Geological Survey of
1235 Finland, Espoo.

1236 Szanyi, J., Rybach, L., & Abdulhaq, H.A. (2023). Geothermal energy and its potential for critical metal
1237 extraction—A review. Energies, 16, 7168. https://doi.org/10.3390/en16207168

1238 Väisänen, M., & Skyttä, P. (2007). Late Svecofennian shear zones in southwestern Finland. GFF, 129, 55–
1239 64. https://doi.org/10.1080/11035890701291055

1240 Viola, G., Mattila, J., Zwingmann, H., Todd, A., & Raven, M. (2011). Structural and K/Ar illite
1241 geochronological constraints on the brittle deformation history of the Olkiluoto Region, southwest Finland.
1242 Posiva Working Report. Posiva Oy, Eurajoki, Finland.

1243 Yan, Q.-H., Chi, G., Wang, H., Liu, B., & Zhang, W. (2025). Formation of a granite-related Sn–Pb–Zn–
1244 (Ag) deposit from three discrete mineralization events around a common magmatic-hydrothermal center
1245 over a span of ~45 million years at Changpu, eastern Guangdong, South China. GSA Bulletin, 137, 1872–
1246 1890. https://doi.org/10.1130/B37696.1

Supplementary Files

This is a list of supplementary files associated with this preprint. Click to download.

- SupplementaryMaterialDetailedMethods.docx